Monthly Notices
of the
ROYAL ASTRONOMICAL SOCIETY

MNRAS **491,** 4925–4948 (2020)
Advance Access publication 2019 November 20

doi:10.1093/mnras/stz3244

Understanding extreme quasar optical variability with CRTS – II. Changing-state quasars

Matthew J. Graham [1]★ Nicholas P. Ross [2] Daniel Stern,[3] Andrew J. Drake,[1] Barry McKernan [4,5,6] K. E. Saavik Ford,[4,5,6] S. G. Djorgovski,[1] Ashish A. Mahabal,[1] Eilat Glikman,[7] Steve Larson[8] and Eric Christensen[8]

[1]*California Institute of Technology, 1200 E. California Blvd, Pasadena, CA 91125, USA*
[2]*Institute for Astronomy, University of Edinburgh, Royal Observatory, Blackford Hill, Edinburgh EH9 3HJ, UK*
[3]*Jet Propulsion Laboratory, California Institute of Technology, 4800 Oak Grove Drive, Pasadena, CA 91109, USA*
[4]*Department of Science, CUNY Borough of Manhattan Community College, 199 Chambers Street, New York, NY 10007, USA*
[5]*Department of Astrophysics, American Museum of Natural History, Central Park West, New York, NY 10028, USA*
[6]*Physics Program, CUNY Graduate Center, 365 5th Avenue, New York, NY 10016, USA*
[7]*Department of Physics, Middlebury College, Middlebury, VT 05753, USA*
[8]*Lunar and Planetary Lab, Department of Planetary Sciences, University of Arizona, Tucson, AZ 85721, USA*

Accepted 2019 November 6. Received 2019 October 10; in original form 2019 May 6

ABSTRACT

We present the results of a systematic search for quasars in the Catalina Real-time Transient Survey exhibiting both strong photometric variability and spectroscopic variability over a decadal baseline. We identify 111 sources with specific patterns of optical and mid-infrared photometric behaviour and a defined spectroscopic change. These 'changing-state' quasars (CSQs) form a higher luminosity sample to complement existing sets of 'changing-look' AGNs and quasars in the literature. The CSQs (by selection) exhibit larger photometric variability than the changing-look quasars (CLQs). The spectroscopic variability is marginally stronger in the CSQs than CLQs as defined by the change in H β/[O III] ratio. We find 48 sources with declining H β flux and 63 sources with increasing H β flux, and discover 8 sources with $z > 0.8$, further extending the redshift arm. Our CSQ sample compares to the literature CLQ objects in similar distributions of H β flux ratios and differential Eddington ratios between high (bright) and low (dim) states. Taken as a whole, we find that this population of extreme varying quasars is associated with changes in the Eddington ratio and the time-scales imply cooling/heating fronts propagating through the disc.

Key words: methods: data analysis – techniques: photometric – surveys – quasars: general.

1 INTRODUCTION

Quasar variability is generally regarded as a stochastic process. The summation of activity associated with accretion disc instabilities, ionizing continua, jets, stellar activity close to the core, and dust clouds is all potential contributor. Sparse studies, either in terms of sample size or temporal sampling, have produced a simple statistical model, the damped random walk (Kelly, Bechtold & Siemiginowska 2009), which aims to describe this variability (but see Zu et al. 2013; Graham et al. 2014; Kasliwal, Vogeley & Richards 2015; Kozlowski 2017; Moreno, Vogeley & Richards 2018; Smith et al. 2018, for counter-discussions). The growing availability of large collections of rich multi-epoch data is, however, enabling a much more phenomenological approach. Systematic studies of the quasar population (or substantial fractions thereof) are now possible with different characterizations of variability in terms of discriminative features or statistical models. These aim to capture specific patterns of behaviour associated with particular underlying physical processes. In this way, we have identified sources exhibiting periodic activity (Graham et al. 2015a,b), major flaring (Graham et al. 2017; Drake et al. 2019), and extreme broad-line variability (Stern et al. 2017, 2018; Ross et al. 2018).

Recent investigations of spectroscopic variability, primarily from dual-epoch SDSS spectroscopy, have reported a number of objects with emerging or disappearing broad emission lines (BELs; prototypically H β) in their optical spectra and often large order of magnitude changes in the optical photometry (LaMassa et al. 2015; MacLeod et al. 2016; Ruan et al. 2016; Runco et al. 2016; Runnoe et al. 2016; Gezari et al. 2017; Assef et al. 2018; Ross et al. 2018; Stern et al. 2018; Wang, Xu & Wei 2018; Yang et al.

★ E-mail: mjg@caltech.edu

2018; MacLeod et al. 2019 (M19)). Such *changing-look quasars* (CLQs) are consistent with a change of spectral type (broad lined to narrow lined or vice versa) and may, in principle, be associated with a large change of obscuration, accretion rate, or accretion disc luminosity. Microlensing is also a potential cause of the CLQ phenomena. The term 'changing-look quasar' is borrowed from X-ray astronomy where large changes in X-ray luminosity have been shown to be typically associated with varying absorption, e.g. Matt, Guainazzi & Maiolino (2003) and Rivers et al. (2015a,b). Similar significant spectral variability has also been known for many years in a number of local low-luminosity active galactic nuclei (AGNs; e.g. Khachikian & Weedman 1971; Tohline & Osterbrock 1976; Penston & Perez 1984; Cohen et al. 1986; Aretxaga et al. 1999; Bischoff & Kollatschny 1999; Eracleous & Halpern 2001; Denney et al. 2014; Shappee et al. 2014; Li et al. 2015; Parker et al. 2016). We note that significant photometric variability and spectroscopic variability have also been detected in quasars with absorption lines systems, e.g. the extreme broad absorption line (BAL) quasar reported by Stern et al. (2017), but such objects are not normally considered as CLQs.

Although this type of behaviour has so far seemed rare, it may well be that data sets are only now sufficient in size and temporal coverage to effectively detect such activity. Runco et al. (2016) studied 102 local ($0.02 \leq z \leq 0.1$) Seyfert galaxies with $M_{\rm BH} > 10^7\,{\rm M}_{\odot}$ and found that ∼66 per cent of objects showed variability (change in values) in width or flux in Hβ over a 3–9 yr timeframe and Hβ completely disappeared in three sources. From a study of SDSS DR7 and DES Y3A1 data for 8640 quasars, Rumbaugh et al. (2018; hereafter, R18) found that ∼ 10 per cent exhibited extreme variability ($|\Delta g| > 1$ mag) sometimes within a 15 yr baseline (the actual distribution of the rest-frame baseline over which the maximum g-band variability was observed peaks around 1000 d but is largely insensitive to time-scales beyond ∼1500 d). Correcting for selection incompleteness, they speculate that 30–50 per cent of all quasars may actually show such a behaviour on these time-scales.

The link between extreme spectroscopic and photometric variability is not clear, however. Despite R18's suggestion that extreme variability quasars (EVQs; $|\Delta g| > 1$) are good candidates for CLQs, a large-amplitude photometric variation alone is not enough to identify them. On the one hand, we have previously reported extreme variability that is not associated with significant spectroscopic changes (Graham et al. 2017). On the other hand, while MacLeod et al. (2016) report on a sample of 10 CLQs with $|\Delta g| > 1$, Yang et al. (2018) present a sample of 21 CLQs, 15 of which have $|\Delta g| < 0.5$ (their full sample spans $0.03 \leq |\Delta g| \leq 1.89$). Therefore, observations show that the spectroscopic CLQ and photometric EVQ phenomena are not directly correlated. What does seem to be indicated is that there are specific *patterns* of variable behaviour that are likely associated with CLQs: for example, Lawrence et al. (2016; hereafter, L16) identify a sample of 15 quasars, including one CLQ, showing slow steady changes over several years, which they attribute to a mixture of changes in accretion state and microlensing. It is also unclear whether CLQs stand out from *single* epoch spectroscopy. L16 report that slow blue hypervariables have weaker Mg II and [O III] emission lines. However, R18 find that EVQs have lower Eddington ratios and larger Mg II and [O III] equivalent widths (EWs) than control quasars matched in redshift and luminosity. Although L16 and R18 form a superset containing some CLQs, they do suggest that quasars with lower accretion rates are more susceptible to changes in accretion rate and exhibiting more extreme behaviour.

Strong correlations are reported as well between CLQ behaviour and mid-infrared (MIR) variability (Sheng et al. 2017; Assef et al. 2018; Yang et al. 2018) with optical and MIR colours also changing with flux variation: a bluer-when-brighter chromaticism in the optical and redder-when-brighter in the MIR. Given the pc-scale size of the MIR-emitting region, this clearly indicates that the strong variability is not due to an obscuring screen. Instead, the chromatic trends are likely due to less host galaxy contributions and a stronger inner accretion disc contribution when quasars are more luminous.

Further evidence against obscuration being the primary cause of CLQs comes from optical polarimetric studies. If the disappearance of the BELs originates from the obscuration of the quasar core by dusty clouds moving in the torus, high linear optical polarization would also be expected. Measurements of the polarization of CLQs (Hutsemekers et al. 2017, 2019; Marin 2017) are less than 1 per cent, which suggests that the phenomenon is not due to obscuration but physical changes in the accretion disc and/or accretion rate. Such low polarization degrees indicate as well that these quasars are seen under inclinations close to the system axis. Finally, imaging of the host galaxies of four faded CLQs (Charlton et al. 2019) suggests that these are predominantly disrupted or merging galaxies that resemble AGN hosts, rather than inactive galaxies.

In this work, we present a search for quasars showing photometric and spectroscopic variability consistent with a change of state of activity. We will refer to these as *changing-state quasars (CSQs)* rather than CLQs. Though the latter has been the conventional term in the literature to date, it is ill-defined with no clear phenomenology, be it photometric or spectroscopic, associated with it beyond 'significant' variability. In the optical community, literature often ascribes variability to either changes in obscuration (as in the X-ray community) or changes in accretion rate, and it has been a challenge to identify physical mechanisms that would lead to accretion rate changes. The significant MIR variability associated with the optical variability in these sources largely rules out the obscuration scenario as already noted. More recently, several papers have noted that the variability events occur on thermal time-scales (Noda & Done 2018; Ross et al. 2018; Stern et al. 2018; Parker et al. 2019), implying that the luminosity changes are likely associated with rapid changes in the temperature of the accretion disc. In contrast, changes in the accretion rate would be expected on the viscous time-scale, which is more than an order of magnitude longer (i.e. decades/centuries rather than years). CSQ is therefore the more appropriate term but we will continue to refer to those objects already identified in the literature as CLQs (see Table A1 and Fig. A1 for those covered by the data used in this work).

This paper is structured as follows. In Section 2, we summarize the data sets used and in Section 3, we present the selection technique and criteria for identifying CSQs. We discuss our results in Section 4. Section 5 considers implications for the physical mechanisms behind the variability. We assume a standard WMAP 9 yr cosmology [$\Omega_{\Lambda} = 0.728$, $\Omega_{\rm M} = 0.272$, and $H_0 = 70.4$ km s^{-1} Mpc^{-1}; Jarosik et al. (2011)], and magnitudes are approximately on the Vega system.

2 DATA SETS

A systematic search for sources showing the particular behavioural patterns associated with CSQs requires a data set with a long temporal baseline and also a high sampling rate. Some candidates may be identified from relatively few epochs of data spread

Table 1. A summary of the selection criteria employed to identify CSQs. Note that sources associated with nearby bright stars or identifiable as blends are removed before cross-matching against MQ.

Selection	Total #
The number of MQ sources with CRTS light curve	1411 364
with more than 10 observations	1143 162
and not a known blazar	1139 438
and outside 95 per cent contour in BB/SWV_1 space	65 816
and $\Delta\|W1\|$ or $\Delta\|W2\| > 0.2$	47 451
and $z < 0.95$	14 412
and has SDSS spectrum	7576
and has second epoch spectrum after $\geq$500 d	717
and H β/[O III] ratio changes by >30 per cent	111

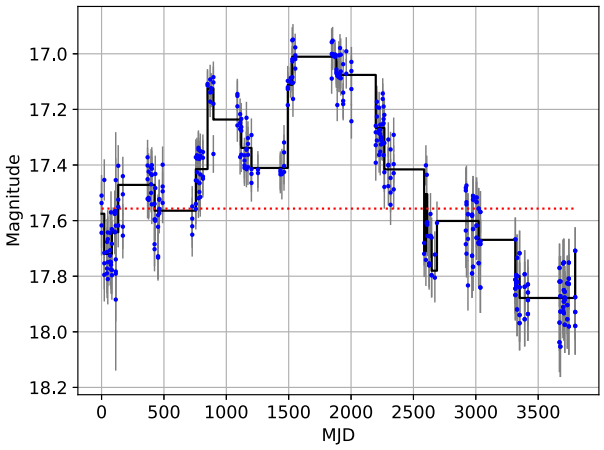

Figure 1. A BB representation of a quasar time series. The red dotted line indicates the median magnitude. The difference between the first and last segments is $\Delta BB = 0.3$ mag.

over a roughly decadal baseline, but such data sets will typically have insufficient resolution or sensitivity to detect specific forms. The Catalina Real-time Transient Survey (CRTS; Drake et al. 2009) represents the best data currently available with which to systematically define sets of quasars with particular temporal characteristics.

2.1 CRTS

The CRTS archive[1] contains the Catalina Sky Survey data streams from three telescopes – the 0.7 m Catalina Sky Survey (CSS) Schmidt and 1.5 m Mount Lemmon Survey (MLS) telescopes in Arizona and the 0.5 m Siding Springs Survey (SSS) Schmidt in Australia. These surveys, operated by the Lunar and Planetary Laboratory at the University of Arizona, were designed to search for near-Earth objects, but have proven extremely valuable for astrophysics topics ranging from galactic transients (Drake et al. 2014) to distant quasars (Graham et al. 2014, 2015b, 2017). CRTS covers up to ∼2500 deg^2 per night, with four exposures per visit, separated by 10 min. The survey observes over 21 nights per lunation. The data are broadly calibrated to Johnson V (see Drake et al. 2013 for details) and the current CRTS data set contains time

[1] http://catalinadata.org

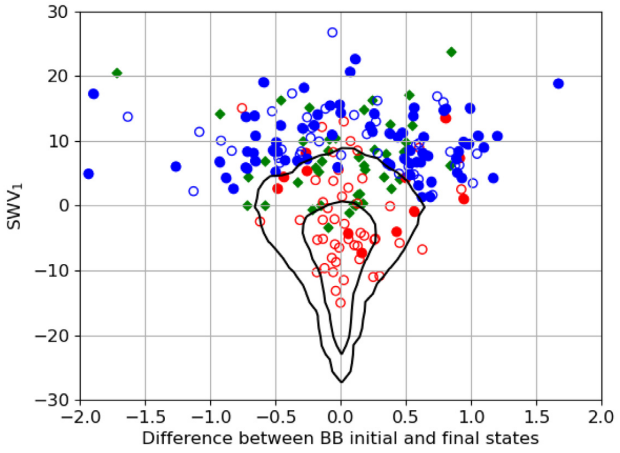

Figure 2. The distribution of the magnitude difference between initial and final BB components and the similarity (aggregate distance) to the median SWV for the quasars in our data set. Known CLQs are denoted by red circles, and blue circles indicate CSQs identified in this work. Open symbols indicate low-luminosity sources with $M_V < -23$. The contours indicate the 68th and 95th percentile levels, respectively, for a population of 128 000 spectroscopically confirmed quasars with $V < 19$. The green diamonds show quasars that have exhibited significant flaring activity (Graham et al. 2017).

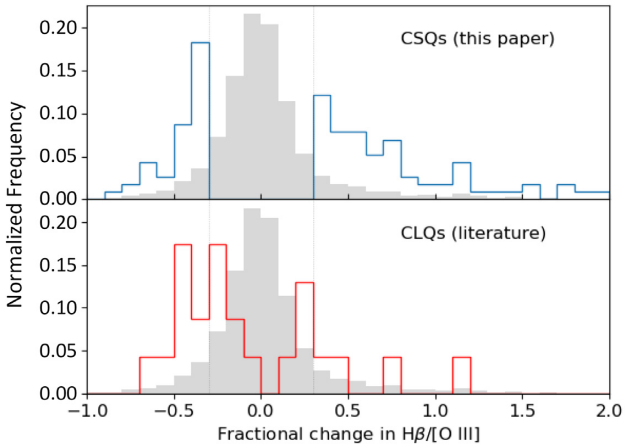

Figure 3. The distribution of the fractional change in the H β/[O III] ratio for SDSS sources (grey) with multi-epoch spectra and H β coverage. The red (bottom panel) indicates the distribution for known CLQs from the literature with publicly available spectra and the blue (upper panel) indicates the CSQs selected here. The dotted lines show the spectroscopic variability selection criteria.

series for approximately 400 million sources to $V \sim 20$ above Dec > -30 from 2003 to 2016 May (observed with CSS and MLS) and 100 million sources to $V \sim 19$ in the southern sky from 2005 to 2013 (from SSS).

The error model used for CRTS DR2 is incorrect: errors at the brighter magnitudes are overestimated and those at fainter magnitudes ($V > 18$) are underestimated (Palaversa et al. 2013; Drake et al. 2014). In this analysis, we employ the improved error model derived in Graham et al. (2017); the actual CRTS error model will be fixed in a future release. We also note that none of the sources we consider have fewer than 10 observations in their light

Table 2. CSQs selected in CRTS and associated features including the median CRTS magnitude (V_m), the optical amplitude (Amp), absolute change in $W1$, Bayesian block change (ΔBB), Slepian wavelet variance measure (SWV_1), and the change in flux ratio of H β to [O III]. SMBH virial mass estimates are calculated as described in Section 5.1.

Name	V_m (mag)	z	log (M_{BH}) ($M_\odot$)	log (L_V) (erg s^{-1})	Amp (mag)	ΔBB (mag)	SWV_1	$\lvert\Delta W1\rvert$ (mag)	Δ(H β/[O III])
SDSS J002331.3+055354.8	18.70	0.637	8.5	44.22	0.44	0.26	7.7	0.37	− 0.75
SDSS J002353.5−025159.1	16.94	0.246	7.5	44.01	0.44	0.81	15	0.44	− 0.31
SDSS J005346.1+223221.9	16.26	0.149	8.4	43.83	0.74	0.57	14	0.48	− 0.36
SDSS J011919.3−093721.6	19.04	0.383	7.4	43.60	0.79	0.84	8.3	0.50	− 0.39
SDSS J012326.8+241844.1	18.40	0.914	9.0	44.76	0.45	0.44	5.2	0.26	3.20
SDSS J022014.6−072859.3	17.02	0.213	7.8	43.83	0.31	− 0.30	12	0.29	0.75
SDSS J024533.6−000745.2	18.64	0.655	8.2	44.27	0.62	− 0.49	9.8	0.27	0.91
SDSS J025003.0+010930.7	17.44	0.194	7.2	43.61	0.46	0.27	13	1.00	0.41
SDSS J025410.1+034912.5	19.03	0.774	8.1	44.34	0.75	− 0.88	4.3	0.53	0.37
SDSS J025505.7+002523.5	18.47	0.353	7.6	43.79	0.77	1.20	11	0.63	− 0.40
SDSS J025619.0−004501.0	19.17	0.723	7.9	44.19	0.87	0.38	11	0.64	− 0.62
SDSS J074542.3+421404.5	17.94	0.268	7.5	43.71	0.56	− 0.83	8.4	0.44	0.65
SDSS J074819.0+335311.0	18.33	0.278	8.8	43.62	1.43	− 0.92	10	0.53	1.58
SDSS J075440.3+324105.1	17.97	0.411	7.7	44.13	0.72	0.26	14	0.30	0.40
SDSS J075728.3+245510.1	18.53	0.187	7.6	43.13	0.73	− 1.08	11	0.34	1.19
SDSS J080138.7+423355.2	19.93	0.771	7.4	43.92	0.98	0.60	3.1	0.72	− 0.35
SDSS J080500.3+340225.6	18.32	0.401	7.3	43.93	0.70	− 0.66	14	0.41	0.66
SDSS J081425.9+294116.3	19.12	0.374	8.0	43.54	0.69	0.71	1.6	0.40	− 0.32
SDSS J081632.1+404804.6	19.73	0.701	8.5	43.92	1.07	0.70	3.7	0.40	− 0.48
SDSS J082033.3+382420.4	18.58	0.648	7.6	44.29	0.52	0.44	11	0.49	− 0.33
SDSS J082930.7+272821.9	18.29	0.321	7.5	43.72	0.53	0.91	6.3	0.57	− 0.40
SDSS J083111.6+345928.1	17.61	0.438	8.8	44.31	0.79	− 0.52	8.5	0.54	0.43
SDSS J083225.3+370736.6	15.52	0.092	–	43.67	0.56	− 0.06	27	0.36	1.89
SDSS J083236.3+044506.2	18.42	0.292	8.2	43.58	0.70	− 0.16	9.9	0.55	0.38
SDSS J083533.2+494818.8	18.49	0.198	7.7	43.19	0.51	− 0.31	7.9	0.89	0.75
SDSS J084716.1+373218.7	17.85	0.454	7.4	44.23	0.41	− 0.07	11	0.31	0.30
SDSS J091357.3+052229.8	19.22	0.346	5.8	43.45	0.64	0.56	4.8	0.64	− 0.57
SDSS J092441.1+284730.6	18.52	0.464	8.3	43.97	0.85	0.53	8.6	0.83	− 0.37
SDSS J092736.7+153824.3	18.25	0.555	7.9	44.26	0.59	− 0.91	8.4	0.45	− 0.32
SDSS J092836.9+474245.8	19.58	0.830	–	44.11	0.83	0.68	1.4	0.73	− 0.77
SDSS J093017.7+470721.7	16.52	0.160	7.3	43.75	0.47	0.28	16	0.48	0.40
SDSS J093329.0+291734.1	17.90	0.262	6.8	43.67	0.54	0.60	9.6	0.76	− 0.48
SDSS J094231.7+233613.6	18.31	0.795	9.6	44.60	1.45	0.89	5.1	0.43	− 0.63
SDSS J094620.9+334746.5	16.19	0.239	7.9	44.26	0.54	− 0.59	19	0.86	0.50
SDSS J095427.6+485638.9	18.47	0.248	8.2	43.38	0.65	1.05	8.0	0.59	− 0.37
SDSS J095536.8+103751.7	17.46	0.284	7.5	43.93	1.08	− 1.90	17	0.52	2.95
SDSS J095750.0+530106.0	18.34	0.437	7.4	43.97	0.85	− 0.20	12	0.57	1.14
SDSS J100256.2+475027.9	18.41	0.391	8.2	43.84	0.69	− 0.65	11	0.49	0.88
SDSS J100343.3+512611.2	18.25	0.431	7.7	43.99	0.51	− 0.43	7.0	0.41	0.39
SDSS J102614.0+523752.0	17.68	0.259	7.4	43.74	0.69	− 0.37	17	0.99	0.35
SDSS J102752.4+421012.5	18.42	0.933	8.4	44.68	0.64	0.93	4.3	0.60	1.13
SDSS J102817.7+211508.1	18.46	0.365	8.3	43.76	0.61	− 0.93	6.8	0.53	0.46
SDSS J103255.9+365451.0	18.91	0.894	8.8	44.45	0.70	− 0.82	2.6	0.35	0.57
SDSS J104254.8+253714.2	18.30	0.603	–	44.33	0.61	− 0.72	8.4	0.23	0.49
SDSS J105907.2+472331.5	17.71	0.212	8.1	43.56	1.11	− 0.53	15	0.42	5.81
SDSS J110349.2+312416.7	20.27	0.438	7.1	43.22	1.02	− 1.13	2.2	2.20	− 0.38
SDSS J110501.3+562723.8	17.80	0.238	8.8	43.62	1.30	1.0	3.5	0.74	0.66
SDSS J111617.8+251035.0	18.36	0.534	8.3	44.16	0.92	0.63	8.1	0.50	− 0.45
SDSS J111930.4+222649.8	17.21	0.420	9.2	44.41	1.21	0.47	11	0.64	0.66
SDSS J111947.6+233539.9	17.65	0.147	7.4	43.22	0.58	0.20	11	0.62	− 0.49
SDSS J112243.1+364141.6	18.15	0.313	7.7	43.74	0.45	− 0.45	8.6	0.57	0.47
SDSS J113111.1+373709.4	18.62	0.448	7.9	43.90	0.76	0.63	11	0.27	− 0.36
SDSS J113706.9+013948.2	16.56	0.193	7.4	43.92	0.42	0.56	15	0.49	− 0.31
SDSS J113757.7+365501.8	18.78	0.861	7.9	44.46	0.85	0.88	7.3	0.37	− 0.30
SDSS J114408.9+424357.5	18.08	0.272	8.6	43.63	0.62	0.88	6.1	0.29	− 0.39
SDSS J115349.3+112830.4	16.20	0.176	9.2	44.00	1.04	0.014	21	0.40	0.47
SDSS J120130.9+494049.8	18.00	0.392	7.6	44.02	0.68	− 0.46	12	0.74	0.39
SDSS J120442.2+275411.6	16.34	0.165	8.0	43.86	0.44	− 0.28	18	0.51	0.58
SDSS J122136.8+343541.4	17.68	0.299	8.4	43.89	1.19	− 0.73	14	0.82	1.54

Table 2 – *continued*

Name	V_m (mag)	z	log (M_{BH}) ($M_\odot$)	log (L_V) (erg s^{-1})	Amp (mag)	ΔBB (mag)	SWV$_1$	$\lvert\Delta W1\rvert$ (mag)	Δ(H β/[O III])
SDSS J122503.4+293931.0	17.09	0.479	9.0	44.59	0.72	0.5	5.9	–	−0.52
SDSS J123001.0+335901.6	16.33	0.448	9.4	44.83	0.56	−0.25	7.2	–	2.80
SDSS J123203.6+200929.5	14.75	0.064	7.4	43.66	0.22	0.45	12	0.45	1.13
SDSS J123215.2+132032.3	17.71	0.286	8.1	43.84	0.45	0.49	7.3	0.67	−0.65
SDSS J123819.6+412420.4	18.94	0.499	8.5	43.88	0.56	0.53	4.8	0.40	−0.39
SDSS J125327.7+145456.2	17.64	0.252	9.3	43.76	1.20	−0.18	14	0.65	3.16
SDSS J130749.6+350140.4	17.02	0.301	8.5	44.15	0.97	0.81	15	0.45	0.35
SDSS J134133.7+090356.3	16.80	0.105	7.4	43.27	0.60	0.74	17	0.81	−0.70
SDSS J134628.4+192243.3	15.54	0.084	8.5	43.58	0.24	0.58	14	0.95	−1.00
SDSS J134822.3+245650.4	17.98	0.293	7.5	43.74	0.45	0.60	4.1	0.47	−0.42
SDSS J135636.6+255320.0	18.91	0.277	7.2	43.32	0.76	0.58	9.3	0.75	−0.41
SDSS J135820.4+134345.9	17.01	0.129	7.6	43.38	0.74	−0.23	10	0.36	1.80
SDSS J140506.2+171708.3	17.44	0.339	9.2	44.13	0.84	0.63	1.3	–	−0.62
SDSS J141403.2+352311.6	15.79	0.057	7.0	43.14	0.25	0.56	7.8	0.58	0.80
SDSS J141758.6+091608.7	17.24	0.139	8.5	43.37	0.27	0.58	7.4	0.75	0.53
SDSS J142725.0+194952.3	14.79	0.110	8.6	44.15	0.31	0.43	8.3	0.46	1.34
SDSS J142852.8+271042.9	17.64	0.445	7.7	44.28	0.55	0.25	11	0.47	0.76
SDSS J143919.4+551318.2	17.85	0.257	8.8	43.68	0.44	0.34	4.9	0.34	−0.53
SDSS J144118.9+485454.8	18.60	0.289	7.0	43.52	0.89	−0.47	6.6	0.78	0.73
SDSS J144202.8+433709.1	17.27	0.231	7.2	43.80	0.93	1.67	19	1.10	−0.70
SDSS J144702.8+273747.2	18.45	0.224	7.6	43.31	0.68	0.99	9.5	0.99	−0.49
SDSS J145022.7+102555.8	17.86	0.790	8.0	44.76	0.70	−1.26	6.0	0.49	3.03
SDSS J145440.4+552432.9	18.15	0.446	8.9	44.08	0.59	0.69	6.5	0.69	1.21
SDSS J145450.0+111433.6	16.20	0.467	9.2	44.93	0.52	−0.082	15	0.10	0.60
SDSS J145755.4+435035.5	18.50	0.528	7.5	44.10	0.51	−0.67	8.1	0.66	0.56
SDSS J150332.1+295024.0	16.06	0.109	8.2	43.61	0.25	0.53	8.3	0.62	1.96
SDSS J151604.3+355025.4	18.39	0.592	7.9	44.26	0.50	0.61	6.7	0.35	−0.34
SDSS J152641.9+163246.3	18.95	0.831	8.6	44.39	0.54	0.44	5.9	0.44	0.52
SDSS J152749.9+084408.6	18.87	0.849	–	44.44	1.24	−1.93	5.0	0.28	0.37
SDSS J153354.6+345504.6	18.79	0.753	8.8	44.34	0.93	1.10	9.0	0.95	−0.35
SDSS J153415.4+303434.5	15.92	0.093	7.3	43.51	0.31	−0.26	14	0.77	0.34
SDSS J153926.8+200256.1	18.85	0.472	8.9	43.91	0.71	0.34	9.5	0.34	−0.77
SDSS J155651.4+321008.9	17.88	0.350	7.8	43.96	0.77	1.05	11	1.50	−0.37
SDSS J155829.4+271714.3	16.69	0.090	7.6	43.19	0.35	0.52	6.0	0.28	−0.46
SDSS J160007.4+111316.5	17.30	0.669	9.0	44.86	1.07	0.22	12	0.39	0.36
SDSS J160030.3+264517.2	18.44	0.737	9.2	44.49	0.36	0.19	5.8	0.27	0.66
SDSS J160743.0+432817.1	18.46	0.596	7.8	44.23	0.69	0.94	9.8	0.92	−0.54
SDSS J160848.2+004148.9	18.81	0.425	8.7	43.91	0.43	0.3	6.3	0.55	−0.78
SDSS J161400.3−011005.1	17.87	0.253	7.6	43.78	0.75	0.99	15	0.99	−0.31
SDSS J161413.2+260415.8	15.35	0.131	8.7	44.10	0.86	0.11	23	0.14	0.35
SDSS J162552.8+125316.6	17.96	0.380	9.3	44.06	0.42	0.43	6.7	0.47	0.38
SDSS J163523.4+263046.7	16.99	0.071	7.7	42.89	0.40	0.21	8.0	0.21	1.74
SDSS J171602.0+311214.1	15.31	0.110	7.8	43.93	0.42	0.00	14	0.22	1.03
SDSS J205032.3−070131.3	16.77	0.169	8.8	43.77	0.40	0.55	6.9	0.55	0.98
SDSS J224829.4+144418.4	18.75	0.424	7.7	43.84	0.28	0.07	6.6	0.25	−0.49
SDSS J230443.6−084110.0	13.56	0.047	7.6	43.86	0.26	−0.01	16	0.86	0.68
SDSS J230702.9+043257.0	14.86	0.042	7.6	43.29	0.42	−0.12	15	0.57	0.57
SDSS J231207.6+140212.8	17.82	0.357	7.7	44.05	0.54	−0.48	8.4	0.19	0.52
SDSS J232256.7+185816.6	16.40	0.142	8.0	43.73	0.86	0.79	16	0.56	−0.87
SDSS J232446.7+140029.5	18.62	0.916	8.5	44.63	0.65	0.80	4.3	0.99	−0.38
SDSS J233136.8−105638.0	17.79	0.373	7.4	44.06	0.44	−0.65	6.9	0.21	1.16
SDSS J235439.1+005751.9	18.92	0.390	8.0	43.66	1.20	−1.63	14	1.50	1.43

curve. We apply the same pre-processing steps described in Graham et al. (2015b) to all light curves, which remove outlier photometry points and combine all exposures for a given night to give a single weighted value for that night. We also remove sources associated with nearby bright stars or identifiable as blends from a combined multimodality in their magnitude and observation position, i.e. the spatial distribution of all points in a light curve is best described by $n > 1$ Gaussians.

2.2 WISE

In this paper, we use MIR *W*1 (3.4 μm) and *W*2 (4.6 μm) *WISE* data from the beginning of the mission in 2010 January through 2017 December, corresponding to the fourth year of *NEOWISE* operations.[2] Note that there is a gap between 2011 February and

[2] http://irsa.caltech.edu/wise

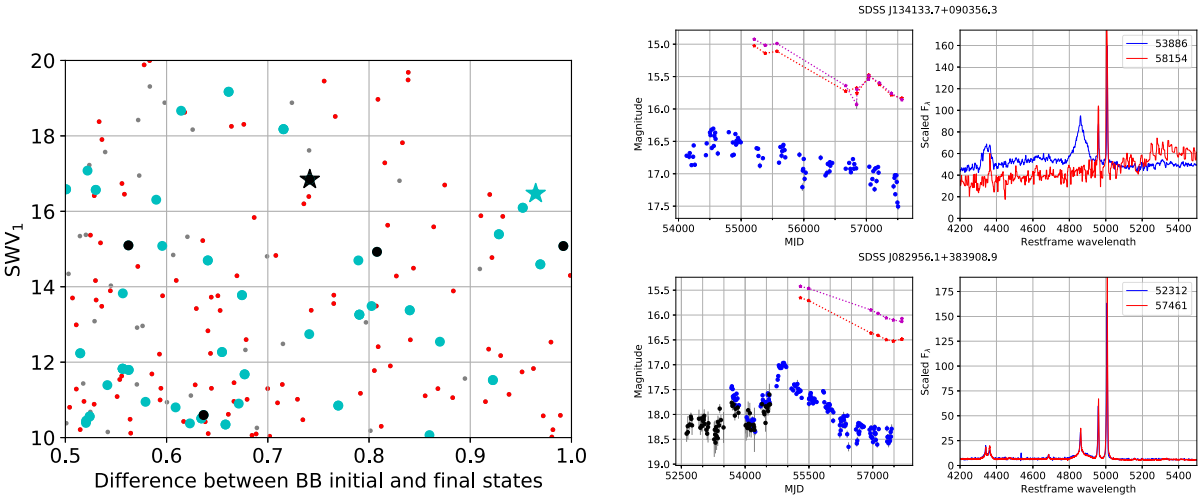

Figure 4. Left: a zoom-in of a region of Fig. 2 showing sources progressively matching the CSQ selection criteria so that each is a subset of the former: red indicates $|\Delta W_{1,2}| > 0.2$, cyan the presence of a second epoch spectrum, and black the significant spectral change in the H β/[O III] ratio. Right: the light curves and spectral region around H β for two candidate CSQs (stars in the left panel). The top shows the data for a CSQ (the black star in the left plot) whilst the bottom shows the same for a source showing no spectral variability (the cyan star in the left plot). It is possible that a spectrum taken at MJD ∼54500 might have shown some variation. The light curves show data from CRTS (blue), LINEAR (black), and WISE (red).

2013 September when the satellite was in hibernation. For most sky positions, there are ∼12 observations of a source over an ∼1 d period with a 6 month gap between repeat visits. We combine all exposures for a given 24 h period with a signal-to-noise ratio greater than 5 to produce a single value using the same method as for CRTS data.

2.3 Spectroscopically confirmed quasars

The Million Quasars (MQ) catalogue[3] v5.2 contains all spectroscopically confirmed type 1 QSOs (577 146), AGN (30 062), and BL Lacs (1615) in the literature up to 2017 August 5. Previous versions have formed the basis for the results of Graham et al. (2015b) and Graham et al. (2017). MQ (v5.2) also contains 1297 111 photometric quasar candidates from SDSS or *WISE*. We cross-matched MQ against the CRTS data set with a 3″ matching radius and find that 1411 364 sources are covered by the full CRTS. Of these, 268 202 do not have enough observations ($n < 10$), leaving a data set of 1143 162 quasars and quasar candidates. We also remove 3724 known blazars based on the class designation in MQ and the BZCAT v5.0 catalogue of blazars (Massaro et al. 2015).

Table 1 gives a summary of this superset of MQ sources to which we now apply our selection criteria to identify CSQs.

3 SELECTING CHANGING-STATE QUASARS

3.1 Optical photometry selection

Photometrically, we expect to see a gradual change in magnitude associated with monotonically varying BEL strengths and/or continuum changes. This would show as a strong localized trend or enhanced variability strength over some time-scale in the time series.

To identify local variability in a time series, we use a Bayesian blocks (BB) representation (Scargle et al. 2013), which provides an optimal segmentation of the data in terms of a set of discontinuous piecewise constant components (see Fig. 1). This approximation makes it easier to detect significant changes of behaviour in the presence of irregular sampling, noise, and gaps. In particular, it is more sensitive to coherent magnitude variations over time characterized by the difference between the first and last piecewise segments of the BB than fitting a linear trend model to the data. We assume it is unlikely that a quasar will undergo a transition and return to its initial state within the timeframe of our light curves. We also distinguish between this pattern of behaviour and flaring as we identified in Graham et al. (2017).

To detect stronger variability on particular time-scales, we use the Slepian wavelet variance (SWV; Graham et al. 2014), which provides a measure of the relative contributions of variability at specific time-scales to the total variability in a time series. We have determined the median observed SWV for quasars in magnitude bins of width $\Delta m = 0.25$. For a given source j, we then calculate the quantity

$$\mathrm{SWV}_{1,j} = \sum_i \left[\log_2 \mathrm{SWV}_{i,j}(\tau_{i,j}) - \log_2 \overline{\mathrm{SWV}}(\tau_{i,j})\right],$$

i.e. the sum of the differences in dyadic log–log space between the source SWV and the appropriate median SWV interpolated at the time-scales of the source SWV. Note that dyadic logs are used since the wavelet bands are defined in terms of base-2 widths.

Fig. 2 shows the distribution of the BB difference and SWV_1 for the quasars in our data set and for known CLQs. We note that using this characterization places the majority (82 per cent) of the known CLQs within the 95th percentile contour. These objects have predominantly been identified from their spectroscopic variability, e.g. from dual-epoch SDSS spectra where the source is classified as a galaxy in one epoch and a quasar in the other. They will thus be in a quiescent galaxy state for at least a fraction of the time period covered by their CRTS light curve (see Fig. A1) and show less photometric variability over this period than the median quasar at the same magnitude. Since our focus is on extreme variability, we only consider sources outside the 95th percentile contour and with

[3] http://quasars.org/milliquas.htm

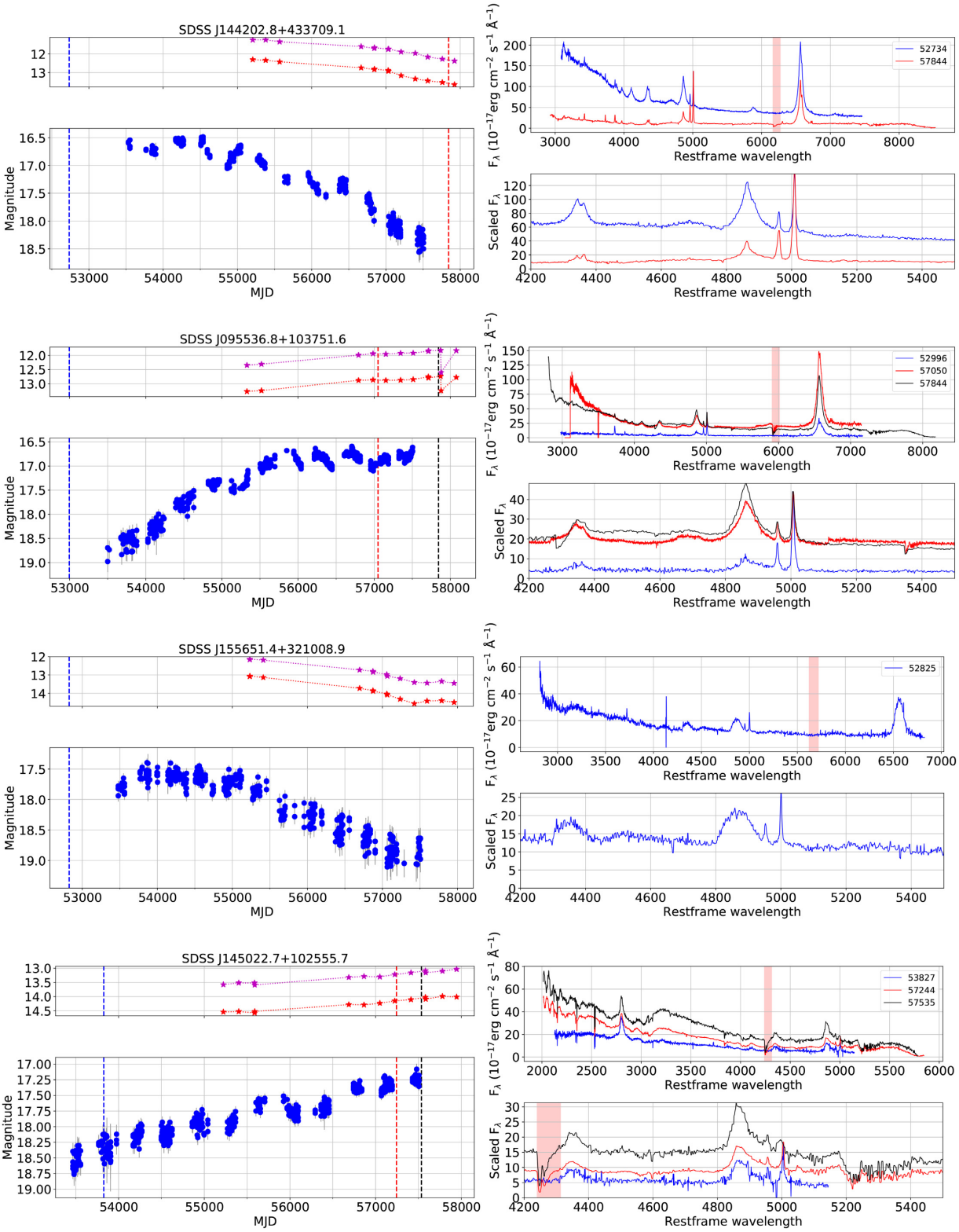

Figure 5. Example light curves and spectra of CSQs identified in this paper corresponding to the largest values in each of the selection parameters: SWV_1, ΔBB, $|\Delta W|$, and ΔH β/[O III] (from top to bottom). The left plot for each source shows the CRTS (blue) data and LINEAR (black) data where available. The *WISE* *W*1 (maroon) and *W*2 (red) light curves are also shown (binned on a daily basis) and offsets ($W1 = 2.70$, $W2 = 3.34$) have been applied to the *WISE* Vega magnitudes for display. The right upper plot for each source shows the SDSS spectra and the spectra obtained in our follow-up. The lower right plot shows a comparison of the H β regions for the spectra scaled to the flux of [O III] λ 5007 in the earliest spectra. The spectra are smoothed with a 3 Å box filter in all cases. The red shaded area indicates the location of the atmospheric O_2 *A*-band absorption feature. The corresponding epochs of the spectra are shown in the left plot by dashed lines.

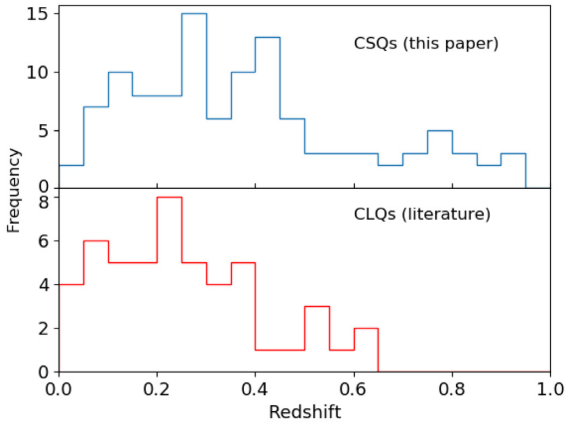

Figure 6. The redshift distribution of known CLQs from the literature (red) and the CSQs selected here (blue).

$SWV_1 > 0$ as candidate objects. The latter criterion selects objects with the above median variability.

3.2 MIR selection

Strong (>0.4 mag) MIR variability has been shown to be a characterizing property of CLQs (Sheng et al. 2017; Assef et al. 2018; Stern et al. 2018) and so we also consider this as a discriminating feature. From the maximum $\Delta W1$ ($\Delta W2$) distribution of MIR variability for quasars over the 7 yr of *WISE* observations, $\Delta m = 0.4$ corresponds to the 82nd (88th) percentile and 3 per cent (3 per cent) of sources vary by more than a factor of two in flux, or $\Delta m > 0.75$, over the period. Yang et al. (2018) argue that a reasonable selection criterion is $|\Delta(W1 - W2)| > 0.1$ when $|\Delta(W1)| > 0.2$ but they define $\Delta(W1)$ as the magnitude difference between the brightest epoch in a *WISE* time series and either the first or last epoch, depending on whether the CLQ is turning on or off. This means that unless the MIR flux is monotonically varying, $\Delta(W1)$ will be some fraction of the total $W1$ variability. It also relies on prior knowledge of whether the CLQ is turning on or off to determine the appropriate magnitude difference to measure. We employ the absolute magnitude difference in a *WISE* time series, i.e. $W_{\rm max} - W_{\rm min}$ as a selection criterion and require either $|\Delta W1| > 0.2$ or $|\Delta W2| > 0.2$ (see Table 1).

The optical variability constraints described above give 65 816 candidates from the initial 1.1 million source data set (rejecting blends) and the MIR variability constraint reduces this to 47 451 sources. Of these, 14 412 have $z < 0.95$ and are therefore suitable for spectroscopic confirmation (i.e. with optical spectroscopy H β falls within the wavelength coverage of the optical spectrum). An SDSS DR14 spectrum exists for 7576 of these and multi-epoch SDSS spectra with at least 100 (500) d between epochs are available for 466 (266) objects. For comparison, there are 213 358 SDSS DR14 (Abolfathi et al. 2017) sources classed as QSOs or AGNs with $z < 0.95$, of which 8213 (4244) have additional spectra taken at least 100 (500) d after the initial epoch.

3.3 Spectroscopic selection

Over the past 3 yr, we have obtained second epoch spectra (all at least >500 d after the initial SDSS epoch) for an additional 426 candidates (and subsequent epoch spectra for another 35 sources) using either the Double Spectrograph (DBSP) on the Hale 200”

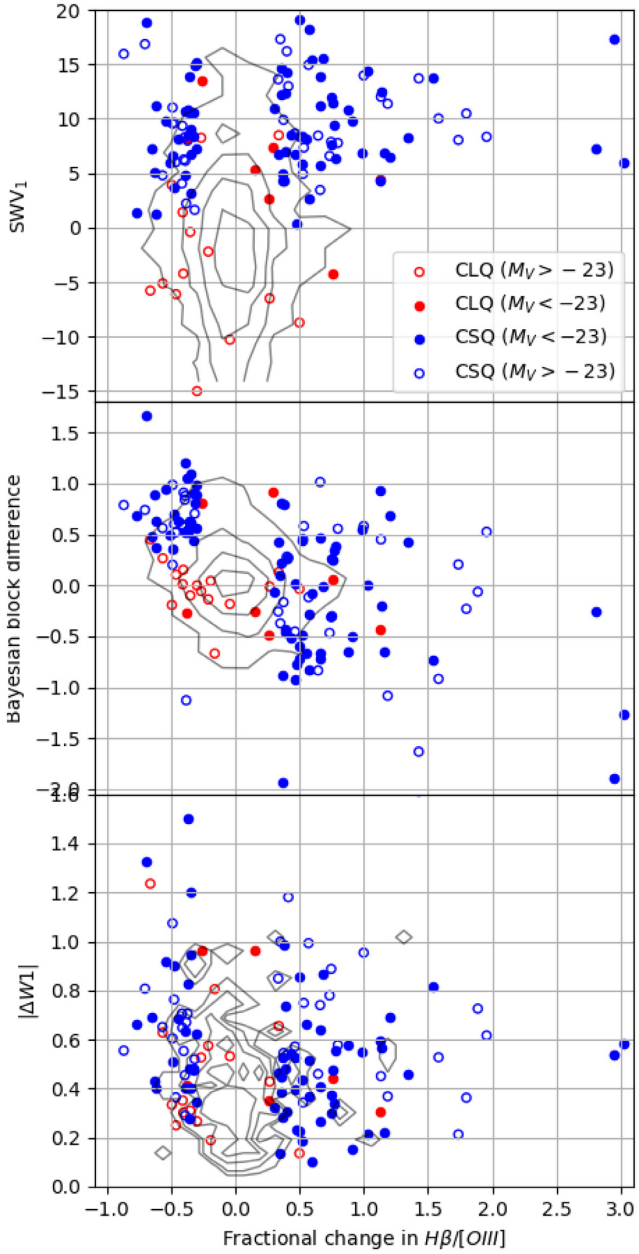

Figure 7. The distributions of the photometric selection criteria – the distance to the median SWV curve, SWV_1, the difference between initial and final BB states, and the maximum W_1 difference – against the spectroscopic variability for the CSQs identified in this paper (blue), known CLQs in the literature (red) where the multi-epoch spectra are available, and the general population of quasars with CRTS light curves (grey contours). Open circles indicate low-luminosity sources with $M_V > -23$. A positive BB difference indicates a transition from a higher (brighter) to a lower (fainter) state. We note that there is one point in the middle panel indicating a source showing a fainter to brighter transition with a decrease in the line ratios: this is J110349+312416 where the second epoch spectrum was taken ∼1000 d before the end of the CRTS light curve. The photometric variability changed after the second spectral epoch and so the two statistics are capturing different behaviour in this source.

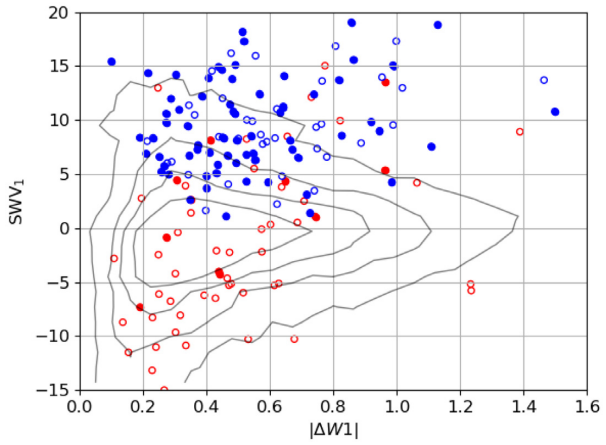

Figure 8. The distribution of optical photometric variability strength against MIR photometric variability. Points are coloured as in Fig. 7.

telescope at Palomar Observatory, the Low Resolution Imaging Spectrometer (LRIS) spectrograph on the Keck I telescope at the W. M. Keck Observatory, or the Echellette Spectrograph and Imager (ESI), also on the Keck I telescope (see Table B1). All these spectra were processed using standard procedures and flux calibrated with observations of spectrophotometric standard stars from Massey & Gronwall (1990) observed on the same night. We fit all spectra with a single power-law continuum and measure H β and [O III] emission line profiles relative to this. We assume a two-component Gaussian fit for H β to model a broad and narrow component and single Gaussians for the [O III] lines. We note, though, that the photometric quality of the nights was not consistent across multiple observing runs, leading to apparent variability in, for example, the strength of narrow [O 3]. With spatial extents up to several kpc, narrow-lined emission should not vary on human time-scales. Some spectroscopic variability is also likely due to different slit/fibre sizes, slit position angles, and seeing variations between observing nights. As discussed below, because of these various issues, our primarily analysis relies on the H β/[O 3], which should be relatively robust to these issues.

There is no objective definition of the spectral variability required to qualify as a CLQ/CSQ in the literature. Some authors (Ruan et al. 2016; Yang et al. 2018) rely on visual inspection to identify sources with obvious broad H β emission in one epoch and no detection in another. MacLeod et al. (2016, 2019) compute the flux deviation between two spectra at any given wavelength to determine the significance of a BEL change and assess the significance of a change relative to the underlying continuum at that wavelength. The earlier work considers a range of significance from $<2\sigma$ change for a faint spectrum to $>8\sigma$, but generally an absence of H β at one epoch is still required. The more recent work assumes a significance in the flux deviation of H β greater than 3. Yang et al. (2018) describe two sources transitioning from type 1 to type 1.8 where H β does not entirely vanish. We can thus define a measure of this deviation to set a lower limit on the change in H β required.

The narrow [O III] λ5007 emission line is not expected to vary on human time-scales and so we can use the change in the flux ratio of H β to [O III] between epochs as a robust indicator of H β change, i.e. the ratio should not be significantly affected by systematic errors due to observing conditions or spectral reduction. Since there is an expectation (almost by definition) that CSQs are associated with significant spectral variability, we will consider only those sources where the absolute value of the fractional change in H β/[O III] > 0.3. We also reject all spectra with a signal-to-noise ratio (SNR) less than 5 as defined in Stoehr et al. (2008) using: SNR $= 0.605 *$ median(f_i)/median($|2f_i - f_{i-2} - f_{i+2}|$), where f_i is the flux at pixel i.

Fig. 3 shows the distribution of the ratio for all SDSS sources with multi-epoch spectra and H β coverage, highlighting known CLQs (bottom panel). Table 2 gives details of the 111 objects that meet our full selection criteria.

4 RESULTS

The light curves and spectra of our final selected sample of 111 CSQs are shown in Fig. B1. We find 48 sources with declining H β and 63 sources with increasing H β. We reject eight sources that meet the photometric selection criteria but have atmospheric O_2 A-band absorption coincident with the H β–[O III] complex in the observed frame.

Fig. 4 shows an example of two sources that pass the photometric selection criteria but only one of which also shows spectroscopic variability. This demonstrates that there is a variety of phenomena that may produce quantitatively similar photometric variability but are distinguishable with multi-epoch spectra. Note that they might also be differentiated by other observables such as X-ray or radio behaviour but this requires further investigation.

Fig. 5 presents the light curves and spectra of CSQs identified in this paper corresponding to the largest values in each of the selection parameters: SWV_1, ΔBB, $|\Delta W|$, and Δ(H β/[O III]. From Figs 5 and B1, we find that extreme variable sources are a heterogeneous population reflecting the complexity of the physics of accretion with subsets dominated by particular processes. Different selection techniques drawing from this population may probe different physics and this needs to be borne in mind in any analysis.

We have identified a sample of CSQs on the basis of excess optical variability over specific time-scales associated with a distinct change in levels of activity over a decade, strong MIR variability, and changes in the strength of H β emission. We are keen to compare this study to previous and contemporary analyses but note that this is not a straightforward exercise. Table A1 and Fig. A1 describe the collective set of CLQs from the literature with CRTS light curves and publicly available spectra. Since these are the result of a variety of selection techniques, we will consider in this section the two samples – CSQs and CLQs – in terms of the selection criteria used in this work.

Fig. 6 shows that the CSQ sample spans a wider redshift range than the known CLQs. The distributions of these two samples as well as the general quasar population in terms of the photometric criteria compared to the spectroscopic are shown in Fig. 7. We also distinguish between low- and high-luminosity sources (taking $M_V < -23$ as the fiducial boundary). The absolute magnitude of a source is given by

$$M_V = m_V - A_V - \mathrm{DM} - K_V,$$

where A_V is the galactic extinction, DM is the distance modulus, K_V is the K-correction, and m_V is the median magnitude from the CRTS light curve. We obtain[4] extinction values at the source position from the Schlafly & Finkbeiner (2011) recalibration of the Schlegel et al. (1998) reddening maps. We assume a K-correction of $K = -2.5(\alpha +$

[4]http://irsa.ipac.caltech.edu/applications/DUST/

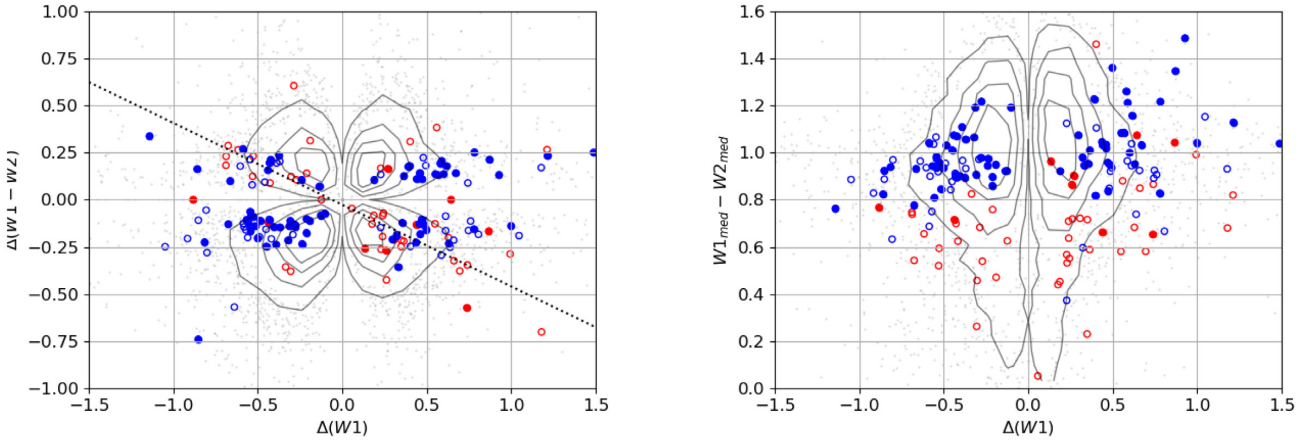

Figure 9. The distribution of MIR colour variability (left) and MIR colour (right) in terms of MIR magnitude variability. The dotted line in the left plot is the brighter-when-redder relationship reported in Yang et al. (2018). The points are coloured as in Fig. 7. The contour lines show the 50th–90th percentiles of the distributions respectively for the general population of quasars with CRTS light curves.

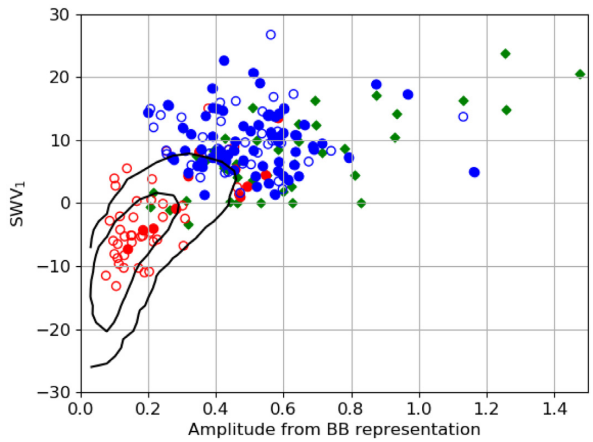

Figure 10. The distribution of the magnitude amplitude from the BB components and the similarity (aggregate distance) to the median SWV for the quasars in our data set. The points and contours are as in Fig. 2.

1)log $(1+z)$ for a power-law spectral energy distribution of $F_\nu \propto \nu^\alpha$ with $\alpha = -0.5$.

It is clear that the CSQ sample represents a more extreme level of photometric variability than the known CLQ set and that the lower luminosity CLQs have a less temporally characterizable variability (smaller SWV_1 values) than their brighter counterparts (Fig. 2). This could be likely due to an overall stronger host contribution to the optical light curve from the generally lower redshift, lower luminosity CLQs as compared to CSQs. The spectroscopic variability also seems marginally stronger in CSQs with objects transitioning from a lower to a higher state of activity, although there is no distinction between high- and low-luminosity sources within this group.

The difference between the initial and final states in the BB representation of the light curve correlates with the fractional change in the Hβ/[O III] ratio, although there is no difference between low- and high-luminosity sources. However, the flux change associated with just Hβ (dis)appearing is not sufficient to account for the full scale of the magnitude change seen in the light curves. Using a composite quasar spectrum, such as Selsing et al. (2016), the magnitude difference for a source with $V \sim 18$ at $z = 0.25$ (which places Hβ roughly at the peak of the CRTS equivalent filter) with and without Hβ is only $\Delta m \sim 0.07$ mag. An accompanying reduction in continuum flux of a third is also required to give a magnitude change of $\Delta m \sim 0.5$, a typical value seen in CSQs. This suggests that there might be quasars experiencing the same physical changes as CLQ/CSQs but which may only exhibit a significant photometric change (corresponding to a change in continuum flux) without showing a corresponding spectral line change, i.e. a population of CLQs without the BEL variability.

There is no correlation, though, between the amplitudes of the MIR photometric variability and the optical spectral variability of these sources (or the general population of quasars). This argues that the physical mechanism underpinning the change of activity manifests differently at the AGN dust torus than at the BEL region, although it is also possible that a correlation does exist but that the different physical locations of the emitting regions within the quasar impose a several years' temporal delay between MIR and spectral variability (e.g. Jun et al. 2015) that simple amplitude measures or the available data do not capture. Fig. 8 shows a trend between the MIR and optical photometric variability for CLQs/CSQs but not for the general quasar population. Since the former are known to show spectral variability, this also supports the idea that continuum variability is the stronger component overall as compared to just spectral line changes.

Yang et al. (2018) reported a 'redder-when-brighter' correlation between MIR colour and magnitude amplitudes, indicative of a stronger contribution from the AGN dust torus when the AGN turns on. Fig. 9 shows that this correlation holds only for the known CLQs and possibly for the lower luminosity CSQs but not for the higher luminosity objects. CSQs are also a redder population at MIR wavelengths than CLQs (a large proportion of which would not pass the MIR selection criteria used in this paper). The higher luminosity, more variable CSQs may thus already have a strong contribution in their MIR flux from the AGN dust torus that the relative change associated with the changing-state mechanism is not so significant an effect as with the lower luminosity sources.

Our selection criteria are somewhat broader by design than those employed in other works, so it is also worthwhile considering CSQs in the context of other criteria used. MacLeod et al. (2019) and other CLQ searches have employed a simple variability amplitude

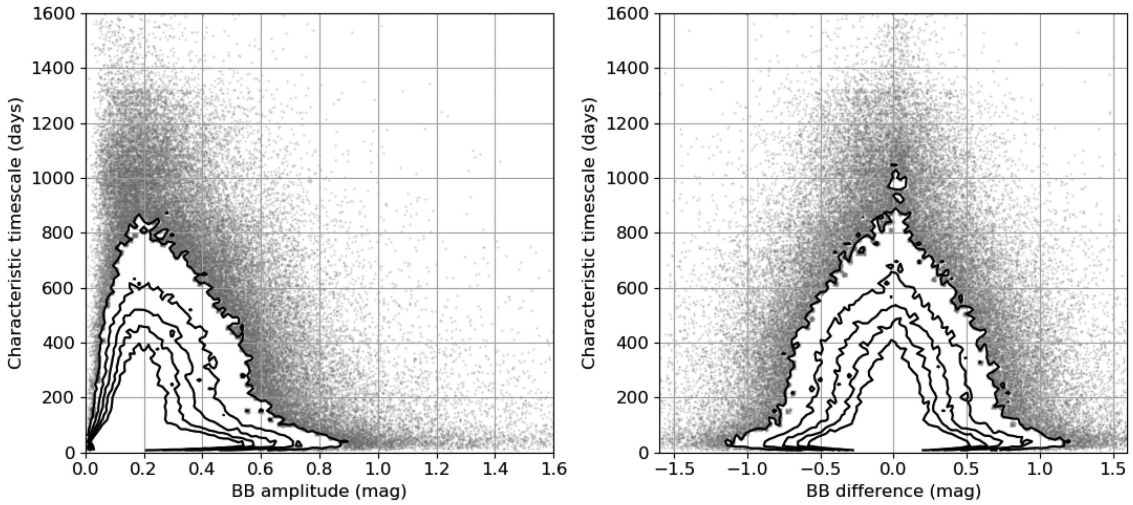

Figure 11. The distributions of the BB amplitude and difference against the characteristic time-scale from the SWV for the initial 1.1 million sources in the MQ superset. The contours show the 50th–90th percentiles of the distributions.

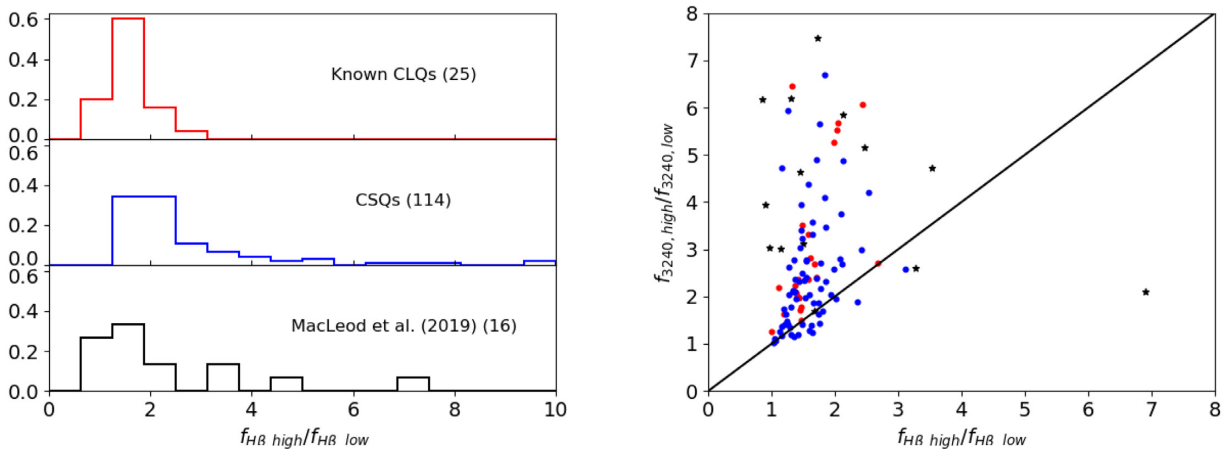

Figure 12. The distributions of the H β flux ratios (left) and H β and continuum (at rest frame 3240Å) flux ratios (right) between the high (bright) and low (dim) states for CSQs (blue), known CLQs with available spectra (red), and the CLQs reported by M19 (black stars). The numbers in the parentheses in the left plot give the number of objects in each data set. The black line with unit slope in the right-hand panel is the expectation for a linear response of BEL flux to the continuum variability (see M19, fig. 4).

criterion (typically $|\Delta g| > 1$) to select sources exhibiting strong photometric variability over any of the available time baselines probed by surveys, such as SDSS and Pan-STARRS 1. We used the difference between the initial and final states of the BB representation of a light curve rather than its amplitude (i.e, the difference between its maximum and minimum states) to identify sources showing significant photometric change but avoiding objects showing flaring activity such as reported in Graham et al. (2017) and Lawrence et al. (2016). Fig. 10 shows that almost all CSQs lie outside the 95th percentile contour in the SWV_1–BB amplitude plane but that flaring quasars from Graham et al. (2017) are the majority source at higher amplitudes (compare with Fig. 2). Known CLQs still form a predominantly less strongly variable population.

It is possible, however, that the long baseline of typically 4000 d between the initial and final states in the observed frame could bias our selection towards quasars with longer time-scale variability and miss shorter time-scale variability potentially associated with CLQs. The SWV measure, SWV_1, has a characteristic time-scale associated with it (see Section 5.2) and Fig. 11 shows the distribution of BB amplitude and difference in relation to this time-scale for the 1.1 million initial sources in MQ. It is clear that with increasing variability, measured either through the amplitude or the difference, there are fewer objects with longer characteristic time-scales and no indication of a selection bias towards them.

The spectral variability constraint (fractional change in H β/[O III] > 30 per cent) that is employed here also differs from the ad hoc visual criteria that have defined CLQs in other searches. As M19 note, the application of such a quantitative definition could lead to a different set of ambiguities and make comparison with other CLQ samples difficult. Fig. 3 shows that our spectral criterion is not met by about 45 per cent of the known CLQs for which we have multi-epoch spectra. CSQs are associated with large continuum luminosity changes and MIR variability over long time-scales but not necessarily with a complete (visual) absence of H β flux in their lower activity (fainter) state. M19 use spectral flux ratios between high (bright) and low (dim) states to determine more clearly how the H β line varies relative to the continuum (measured at rest

frame 3460 Å). They show that strong Balmer line variability is associated with the largest continuum variations but consider their sample too small to determine whether the relative ratio changes are proportional with a constant EW and spectral energy distribution during the transition. Fig. 12 shows that the distribution of H β and continuum (measured at rest frame 3240 Å) flux ratios for CSQs is consistent with the known CLQs for which multi-epoch spectra are available, and the values reported by M19. Note that flux ratios measured for sources where H β has largely disappeared in the low state will be a lower limit. The distribution of values also suggests statistically that the linear response model is supported. This is consistent with the recent results of Gaskell et al. (2019) showing that anomalous broad-line region responses are common events found in the majority of reverberation-mapped AGNs indicating a poor correlation between optical continuum variability and the ionizing continuum variability. This may be due to anisotropic and non-axisymmetric emission in the AGN.

A further complication can arise due to the timing of, e.g. spectroscopic follow-up observations for candidates. Given the data-taking, it is not always possible to obtain a spectrum and sample the light curve, say, at the largest amplitude of variability (in flux, BB, or SWV_1 parameter space). This could present a bias for/against a particular class of object depending on when the spectra are obtained relative to the light curve. We do not claim completeness in our sample: for example, we note that the changing source SDSS J2232-0806 (Kynoch et al. 2019) is a photometric candidate in this work but lacks a second epoch spectrum in our data set. Similarly, 57 of the 262 CLQ candidates (22 per cent) from MacLeod et al. (2019) also appear in our sample of CSQ candidates with single-epoch spectra.

More generally, we can consider our sources in the context of the EVQs of R18. In a comparison with a control sample of SDSS quasars matched in redshift and g magnitude to their EVQ sample, R18 find that EVQs have a larger variability amplitude (from the structure function) than control quasars at all time-scales from days to years. This is equivalent to the SWV_1 selection criteria we have employed with the source SWV_1 greater than the median SWV_1 at the source magnitude across time-scales. However, we compare CSQ quasars to the general population of MQ sources with CRTS light curves rather than a magnitude and redshift-matched sample.

5 DISCUSSION

5.1 Luminosity

Quasar variability is known to be anticorrelated with luminosity in that low-luminosity quasars have a larger probability of showing large-amplitude variation over multiyear time-scales (e.g. Hook et al. 1994; R18). Using the 5100 Å continuum luminosity as a proxy for the intrinsic AGN luminosity, MacLeod et al. (2016) have shown that CLQs seem to preferentially be low-luminosity AGNs (LLAGNs). Fig. 13 shows the distribution of the peak [O III] luminosity from multi-epoch spectra as a function of redshift for the CSQs reported here, the known CLQs, and values measured for 30 000 SDSS quasar at $z < 0.95$. Our CSQs expand the range of changing AGN to more luminous sources and higher redshifts. Furthermore, this type of variability is not dependent on the luminosity of the object.

R18 find that there is a trend of decreasing Eddington ratio with variability. To determine the population distribution, we have

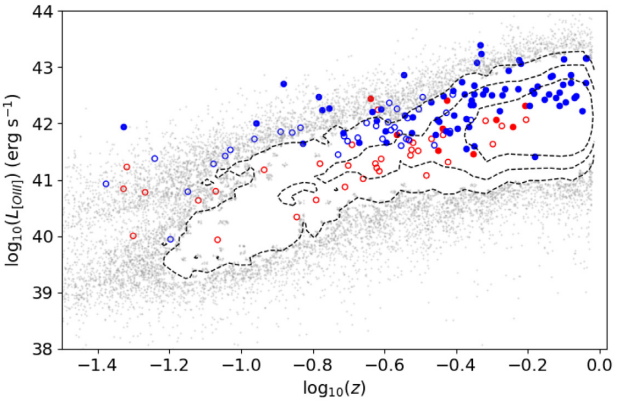

Figure 13. The distribution of the peak [O III] luminosity as a function of redshift. The points are coloured as in Fig. 7. The contour lines indicate the 50th, 70th, and 90th percentiles, respectively.

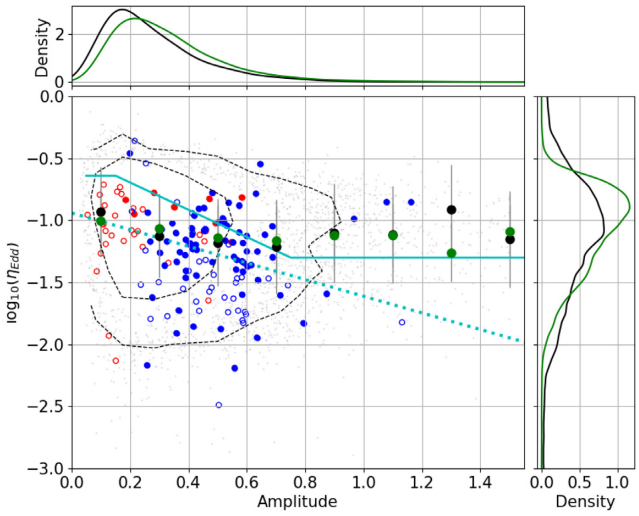

Figure 14. The distribution of Eddington ratio as a function of variability amplitude for SDSS quasars with $z < 0.95$ and multiple spectra separated by more than 500 d (contours and grey points; contours show 68th and 95th percentiles). The black points show the median value for this data set in each bin of variability and the green show the same quantity for all SDSS DR12 quasars from Kozlowski (2017) with $z < 0.95$. The values of known CLQs (red) and the CSQs (blue) reported here are also shown. The solid cyan line indicates the Eddington ratio trend from R18 fig. 10 and the dashed cyan line shows a linear fit to the CLQ/CSQ sources.

calculated the bolometric luminosity for the 4244 SDSS quasars with possible H β coverage ($z < 0.95$) and at least 500 d between multi-epoch spectra using

$$L_{\mathrm{bol},V} = b_V L_{\odot,V} 10^{(M_{\odot,V} - M_V)/2.5},$$

where the solar constants for the V band are $M_{\odot,V} = 4.83$ and $L_{\odot,V} = 4.64 \times 10^{32}$ erg s^{-1} and b_V is the bolometric correction. A comparison with the bolometric luminosities calculated for DR12 quasars from SDSS by Kozlowski (2017) (hereafter K17) with $L_{\mathrm{bol},V}$ gives a mean bolometric correction of $\log_{10} b_V = 1.46$, which we use as a fiducial value hereafter. We estimate the black hole virial mass using

$$\log\left(\frac{M}{\mathrm{M}_\odot}\right) = a + b\log\left(\frac{L_{5100}}{10^{44}\,\mathrm{erg\,s^{-1}}}\right) + 2\log\left(\frac{\mathrm{FWHM(H}\beta)}{1000\,\mathrm{km\,s^{-1}}}\right)$$

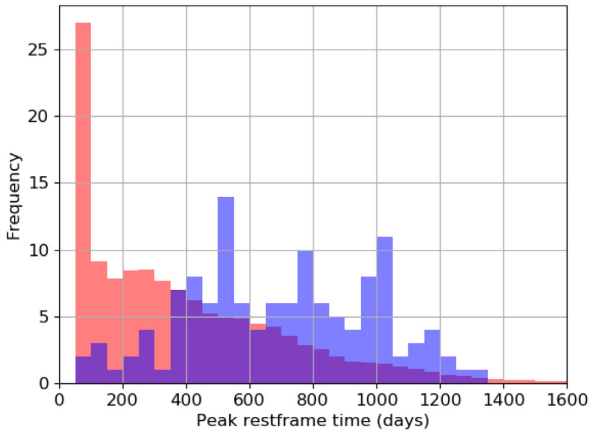

Figure 15. The distribution of the peak rest-frame time-scale contributing to the source variability as measured from SWV. The blue bars indicate the peak time-scale from CSQs/CLQs whilst the red bars show the distribution of peak time-scale for 136 000 quasars with $z < 1.1$ normalized to the CSQ/CLQ sample size.

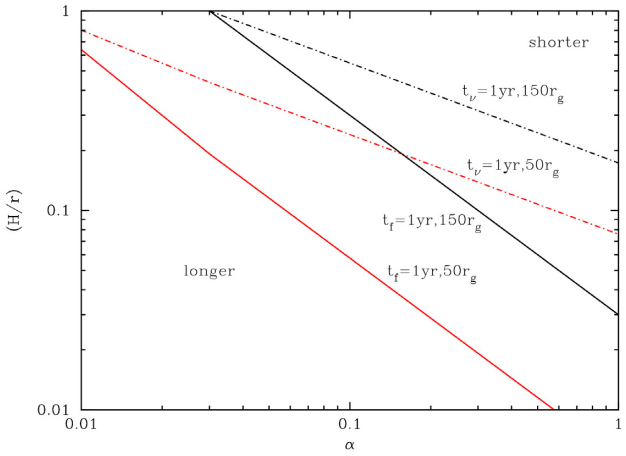

Figure 16. Loci of time-scales from equations (2) (thermal front time-scale; solid lines) and (3) (viscous time-scale; dash–dotted lines) plotted as a function of both α and (h/R). We assumed a fiducial time-scale of 1 yr in each case, at disc radii 50 r_g (red) and 150 r_g (black) around a black hole of mass $M_{\rm BH} = 10^8$ M$_\odot$. If time-scales are shorter, the curves will shift in parallel towards the top right of the figure. If the time-scales are longer, the curves will shift in parallel towards the bottom left of the figure. As the disc approaches a spherical configuration ($H/r \rightarrow 1$), $t_{\rm front} \rightarrow t_{\rm v}$ as we see from equations (2) and (3) and the curves meet. Note that the thermal time-scale in equation (1) is independent of H/r and would therefore correspond to a vertical line at $\alpha = (0.16)\,0.03$ at $(50)\,150\,r_g$.

with $a = 6.91$ and $b = 0.533$ for H β (Ho & Kim 2015). We find that estimates for the same source from multi-epoch spectra are typically consistent within 0.4 dex.

The Eddington ratio is defined as $\eta_{\rm Edd} = L_{\rm bol}/L_{\rm Edd}$, where $L_{\rm Edd}$ is the Eddington luminosity. Fig. 14 shows the distribution of the Eddington ratio for this sample as a function of variability amplitude as measured from the BB fits to the respective time series [note that here amplitude = 0.5 × (max. value − min. value)]. It also shows this distribution for SDSS quasars with potential H β coverage ($z < 0.95$) with Eddington ratio estimates derived as above and also from K17 as a consistency check. The general population does not show any strong indication of decreasing Eddington ratio with increasing variability, as had been previously reported (e.g. R18). Instead, we find that low-amplitude (amp < 0.2) low-luminosity sources have a fractionally higher Eddington ratio ($\eta_{\rm Edd} = 0.2$) relative to an otherwise flat relationship between Eddington ratio and variability amplitude. We note that R18 used Eddington ratio values from Shen et al. (2011) whereas K17 derived their values from their Mg II and C IV-based black hole virial mass estimates. Our values are based on our own H β virial mass estimates and a bolometric luminosity correction derived from K17 data. Although virial mass estimators based on different lines can systematically disagree, this is not sufficient to explain this difference.

The discrepancy may lie in the R18 control sample having no upper redshift bound (the majority of their comparison sample is at $z > 1$) whereas both our CSQs and the control sample data are constrained to $z < 0.95$. There is a correlation between bolometric luminosity (Eddington ratio) and redshift in the R18 sample so that low variability amplitude bins in R18 will be biased towards higher Eddington ratio as a large fraction of objects will have $z > 1$. Higher amplitude bins have comparatively more sources with $z < 1$ and so are more consistent with our results. However, we agree that CLQs/CSQs do show the reported anticorrelation between Eddington ratio and amplitude of variability and that it is stronger for low-luminosity ($M_V < -23$) sources. This is consistent with attributing the changes seen to accretion physics occurring preferentially in lower activity systems but not necessarily just in low-luminosity sources. We also note, though, that although the CSQ (this paper), CLQ (M19), and EVQ (R18) samples all have $\log(\eta_{\rm Edd}) = -2$ to -0.5, this does not imply the same physical mechanisms are necessarily involved across these samples.

5.2 Time-scales

One of the selection criteria in Section 3 was an excess of variability relative to a median level for a magnitude range as measured by SWV. We employed a cumulative measure looking for an overall significant signal rather than one at any specific time-scale. However, CSQs display a particular pattern of activity over the period covered by their light curve and therefore the time-scale that contributes most to the variability of the source should be associated with (or even characteristic of) the physical mechanism driving the change. We have determined the rest-frame time-scale for each CSQ in our data (and CLQ in the literature) at which the SWV of the source has its largest value relative to the median value (see Fig. 15) as well as the distribution of such time-scales for 137 000 quasars with $z < 1.1$. The distribution of peak time values for the CSQ/CLQ sample is significantly different than the population distribution ($>>5\sigma$ according to the Anderson–Darling test) and so the time-scales are indicative of process(es) associated with the observed variability.

As given in Stern et al. (2018), the relevant disc time-scales for a black hole of mass $M_{\rm BH}$ at $R \sim 150\,r_{\rm g}$ can be parametrized as

$$t_{\rm th} \sim 1\ {\rm yr} \left(\frac{\alpha}{0.03}\right)^{-1} \left(\frac{M_{\rm BH}}{10^8\ {\rm M}_\odot}\right) \left(\frac{R}{150\,r_g}\right)^{3/2} \quad (1)$$

$$t_{\rm front} \sim 20\ {\rm yr} \left(\frac{h/R}{0.05}\right)^{-1} \left(\frac{\alpha}{0.03}\right)^{-1} \left(\frac{M_{\rm BH}}{10^8\ {\rm M}_\odot}\right) \left(\frac{R}{150\,r_g}\right)^{3/2} \quad (2)$$

$$t_{\rm v} \sim 400\ {\rm yr} \left(\frac{h/R}{0.05}\right)^{-2} \left(\frac{\alpha}{0.03}\right)^{-1} \left(\frac{M_{\rm BH}}{10^8\ {\rm M}_\odot}\right) \left(\frac{R}{150\,r_g}\right)^{3/2}, \quad (3)$$

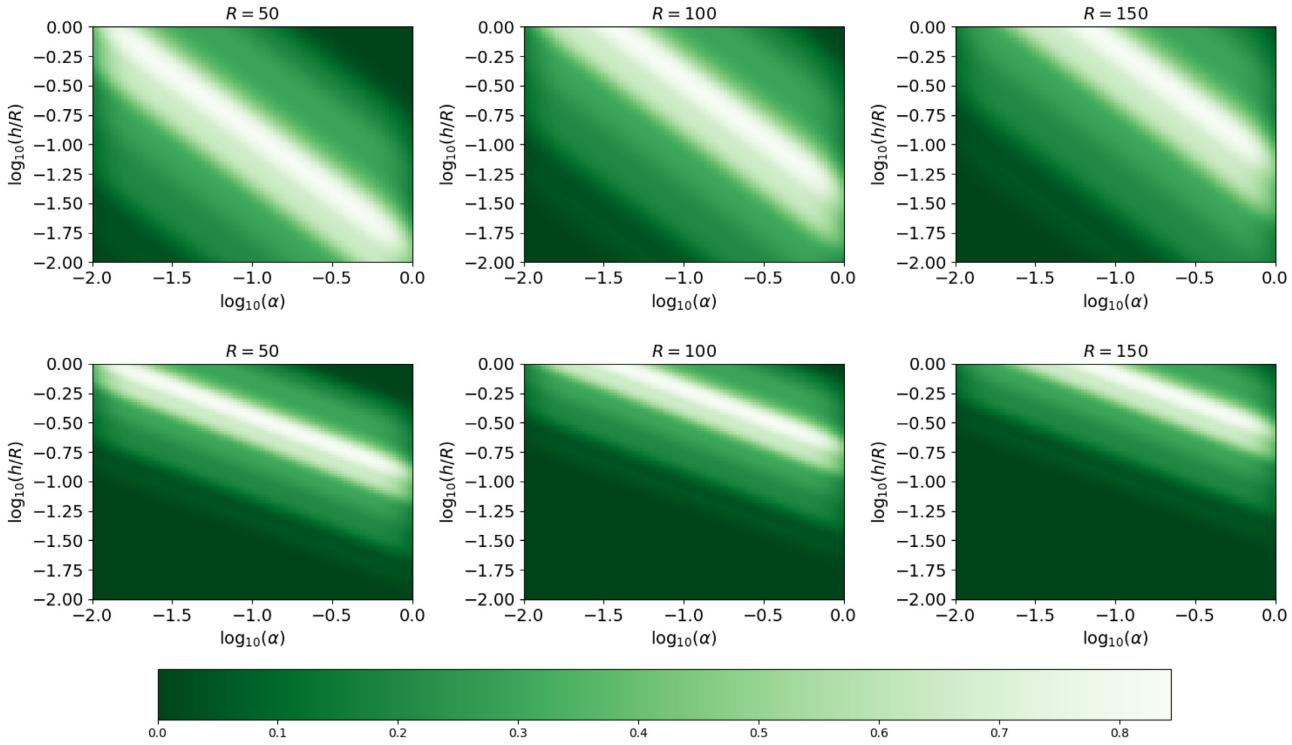

Figure 17. The distribution of $t_{\rm front}$ (top) and $t_{\rm v}$ (bottom) time-scale curves in the h/R–α plane for the CSQ/CLQ sample at values of $R = 50$, 100, and 150 r_g, respectively. Brighter colour indicates denser distribution. Observations and simulations broadly support values of α in the range $0.03 \lesssim \alpha \lesssim 0.5$.

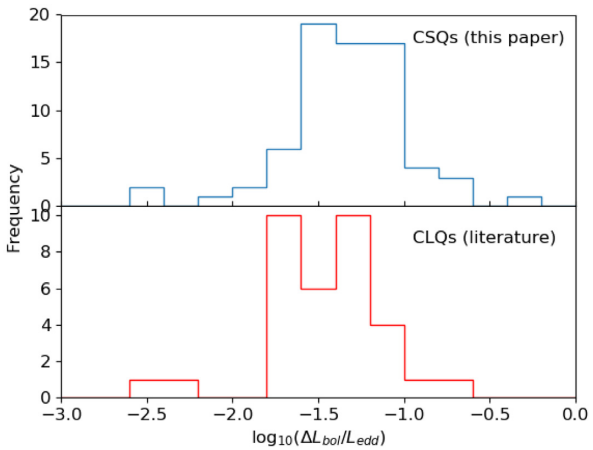

Figure 18. The difference in Eddington ratio associated with the highest and lowest states in the BB representation of a light curve. Known CLQs are shown in red and CSQs in blue.

where α is the disc viscosity parameter, h/R is the disc aspect ratio, R is the disc radius, and $r_g = GM_{\rm BH}/c^2$ is the gravitational radius. The thermal time-scale $t_{\rm th}$ corresponds to the time-scale on which the disc heats or cools with cooling and heating fronts crossing the disc of time-scales of $t_{\rm front}$. The viscous disc time-scale, $t_{\rm v}$, gives the characteristic time-scale of mass flow.

From equations (1)–(3), time-scales associated with processes in AGN discs are expected to be functions of the disc aspect ratio (h/R), disc viscosity parameter (α), black hole mass $M_{\rm BH}$, and disc radius [$R(r_g)$]. In Fig. 16, we show the loci of time-scales from equations (2) and (3) as a function of both α and (h/R). The solid lines correspond to $t_{\rm front} = 1$ yr and the dash–dotted lines correspond to $t_{\rm v} = 1$ yr located at $50r_g$ (red) and $150r_g$ (black), respectively, in a disc around a $M_{\rm BH} = 10^8\,{\rm M}_\odot$. We can read Fig. 16 as follows: if a CSQ is observed to change state on a 1 yr time-scale and we model the associated spectral change with the propagation of a front from the innermost stable circular orbit (ISCO) to $150r_g$, then disc properties (h/R, α) must live on the black solid line (e.g. both $h/R \sim 0.1$, $\alpha \sim 0.3$) and $h/R \sim 0.3$, $\alpha \sim 0.1$ are possible solutions for the model. Likewise, if a CSQ varying on a time-scale of 1 yr is modelled in terms of a viscous change at $50r_g$, then the disc parameters (h/R, α) must live on the red dash–dotted line (e.g. $h/R \sim 0.5$, $\alpha \sim 0.04$ is a possible solution).

For a given value of R, each quasar will define a curve in the (h/R, α) plane and Fig. 17 shows the distribution of these for $t_{\rm front}$ and $t_{\rm v}$ for the CLQ/CSQ sample. There are clearly different preferred regions of the parameter space depending on whether the time-scales are interpreted as front crossing or viscous. For example, King et al. (2007) argue that observations favour a typical range of $\alpha \sim 0.1$–0.4 and this would suggest disc scale ratios of $\sim$0.03–0.1 at $R = 50\,r_g$ for front crossing time-scales but ratios of $\sim$0.2–0.3 for viscous time-scales. Numerical simulations, however, favour $\alpha \sim 0.03$ (e.g. Hirose, Blaes & Krolik 2009; Davis, Stone & Pessah 2010) and thus very thick discs. Although there are degeneracies, broad constraints can be placed on viable disc geometries: a viscous time-scale process favours a thicker disc and less change in disc thickness with increasing radius whereas a front crossing process can support not only a thinner disc but also one that expands more in height with increasing radius.

5.3 Physical mechanisms

Cooling fronts have been proposed as the mechanism for CLQs/CSQs, either as a result of a sudden change in torque applied

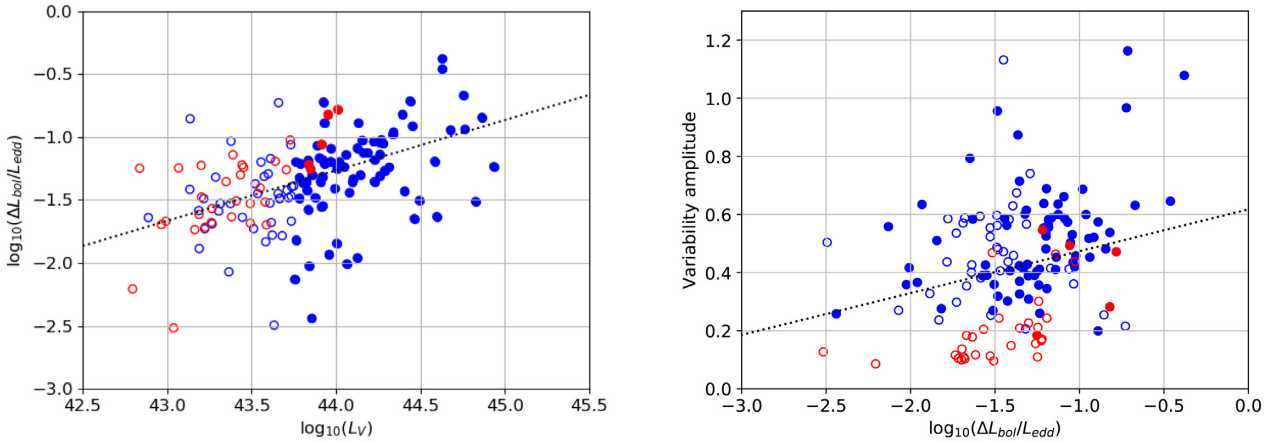

Figure 19. The change of accretion rate (difference in Eddington ratio) associated with the photometric variability as (left) a function of median luminosity and (right) variability amplitude. The same colour scheme is used as in Fig. 7. The black dotted line is the Theil–Sen linear fit to the data. Both distributions favour a linear model over a constant model (no trend) with $p < 10^{-4}$ from the F-test.

Table 3. A summary of the relationships shown for high- and low-luminosity subsets.

Sample	$amp \propto \Delta\eta_{\rm Edd}$ (Fig. 19 R)	$\log(\Delta\eta_{\rm Edd}) \propto L$ (Fig. 19 L)	$\log(\eta_{\rm Edd}) \propto 1/amp$ (Fig. 14)	$L \propto 1/\eta_{\rm Edd}$ (Fig. 20)
Low luminosity	No	Yes	Yes	No
High luminosity	Yes	Yes	No	$L \propto \eta_{\rm Edd}$

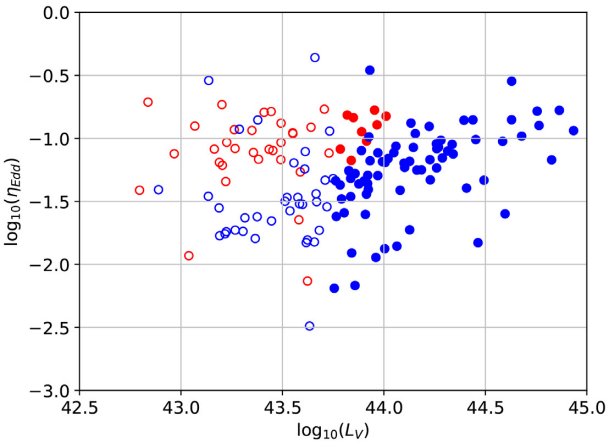

Figure 20. Eddington ratio as a function of luminosity. The same colour scheme is used as in Fig. 7.

by the magnetic field at the ISCO (Ross et al. 2018), or a drop in mass accretion rate causing an advection-dominated accretion flow (ADAF) in the inner disc and spectral state transition by disc evaporation (Noda & Done 2018). Sniegowska & Czerny (2019) also propose that for sources operating at a few per cent of the Eddington limit, there is a radiation pressure instability in a narrow zone between the outer cold gas-dominated disc and an inner hot ADAF flow, which can lead to outbursts producing changing-look behaviour. Noda & Done (2018) suggest that CLQ/CSQ sources can be placed in one of three groups, depending on which particular aspect of the process they exhibit: (1) a factor of two to four decrease in luminosity associated with disc evaporation/condensation; (2) large mass accretion rate change due to thermal front propagation; and (3) a variability amplitude of more than 10 indicative of both phenomena. Most objects should be in either the first or third group, whereas the second group will contain sources showing large variability but not showing any significant spectral changes (although given the results of Section 4, MIR variability would be expected to be shown in addition to optical).

Fig. 18 shows that most CSQs/CLQs are associated with a change of Eddington ratio (accretion rate) of between 1 and 10 per cent $L_{\rm edd}$, consistent with the observational predictions from Noda & Done (2018) and placing these sources in their third group. We note as well (see Fig. 19 and Table 3) that the magnitude of the change in $\eta_{\rm Edd}$ shows a trend with (median) luminosity and also with the amplitude of variability: $amp \propto \log(\Delta\eta_{\rm Edd})$ and $\Delta\eta_{\rm Edd} \propto L/\log(\eta_{\rm Edd})$, where the inverse relationship comes from Section 5.1. In other words, more extreme variability is associated with not only larger changes of $\eta_{\rm Edd}$ in higher luminous systems but also lower actual $\eta_{\rm Edd}$ or, conversely, lower luminosity systems with higher $\eta_{\rm Edd}$ but only able to support a smaller change in $\eta_{\rm Edd}$. If the magnitude of the change in $\eta_{\rm Edd}$ correlates with either a change in torque at the ISCO or a change in mass accretion rate, then larger systems show stronger fluctuations. This suggests that disc instabilities, e.g. magnetohydrodynamical, may be a more likely cause than local perturbative events in the disc, e.g. an embedded supernova, since the latter should not scale with the size of the accreting system. Such instabilities may be driven by the larger environment: Charlton et al. (2019) reported that four CLQs are associated with galaxy mergers, and Kim, Yoon & Evans (2018) have proposed that changing-look activity in Mrk 1018 is due to a recoiling supermassive black hole (SMBH) perturbing the accretion flow on a 29 yr period. Alternatively, both disc instabilities and local perturbative events may be present but with a bias for the latter in lower luminosity systems.

We expect that LLAGN (open circles in Figs 7–20) should be more heterogeneous in origin than the high-luminosity AGN popu-

lation (filled circles in Figs 7–20). This is because either the intrinsic SMBH mass is lower than for the higher luminosity population even if $\eta_{\rm Edd}$ is comparable, or because $\eta_{\rm Edd}$ is intrinsically lower than for the higher luminosity population, or some combination of these. So, we should anticipate a lack of correlation between luminosity among the LLAGN and $\eta_{\rm Edd}$. This is confirmed in Fig. 20 where the LLAGNs (open circles) form a scatterplot. Conversely, for the high-luminosity AGN, there is an apparent correlation with $\eta_{\rm Edd}$ above $\sim 10^{44}$ erg s^{-1} in Fig. 20. While we expect LLAGNs are more heterogeneous than the high-luminosity AGN, a change in the accretion rate in LLAGN (effectively a change in $\eta_{\rm Edd}$) should correlate with luminosity. This is indeed apparent in the left-hand panel of Fig. 19. The LLAGN variability amplitude anticorrelates with the accretion rate (Fig. 14), which suggests that it is harder to significantly change the accretion rate in LLAGN.

6 CONCLUSIONS

We have identified 111 quasars exhibiting strong coherent optical and MIR photometric variability with significant contemporaneous spectroscopic variability that are comparable to the ∼60 existing CLQs reported in the literature. Our sample, however, forms a higher luminosity (and higher redshift) counterpart to the known CLQs showing that this phenomenon is not restricted to low-luminosity systems. The characterizing preference is rather for systems with low Eddington ratios and with the amplitude of the associated variability correlated with a change of Eddington ratio. Characteristic time-scales of the photometric variability suggest that it most closely matches the time-scale associated with a cooling/heating front propagating through the disc as has been proposed for individual sources (Noda & Done 2018; Ross et al. 2018; Stern et al. 2018). The lack of large variability in smaller systems may also indicate disc instabilities associated with magnetic phenomena as the more likely physical cause for the fronts, particularly in larger systems.

The next generation of sky surveys, such as the Zwicky Transient Facility (Bellm et al. 2019; Graham et al. 2019) and LSST, will effectively monitor all AGNs in the sky over few nights. Generative models of quasar variability can be learned from archival data and predicted behaviour compared to that observed with unexpected changes identified far more quickly – in weeks or months rather than years – than waiting for a significant magnitude change to be detected. In this way, these changes of the state of the accretion disc can be tracked with follow-up resources as they happen rather than serendipitously or after the fact. This will allow us to test more easily the theoretical explanations for these phenomena.

Future work will employ machine learning to identify potential further sources – the combination of known CLQs and the CSQs reported here ensures that there is now adequate coverage of the parameter space and a suitable training set can be defined. Further characterization of the sources will also aid this activity. We have also undertaken a program to find CSQs with $z > 0.95$, i.e. where H β does not fall into the optical spectral range. Candidates sharing the same photometric variability as their lower redshift counterparts have been identified and optical and near-IR spectra are being obtained, the latter to capture H β. Although multi-epoch near-IR spectra are unlikely to exist, we will explore the possible correlations between Mg II and H β variability for these sources relative to a more expected lack of correlation in the general population. We are interested as well in those objects that meet the photometric selection criteria but not the spectroscopic to understand if we are probing the same population but missing the spectral variability due to delayed discovery and follow-up or whether such objects are associated with a different phenomenon. Similar efforts are underway for sources with mid-IR variability but no associated optical change.

ACKNOWLEDGEMENTS

We thank Chelsea MacLeod for useful discussions.

This work was supported in part by the NSF grants AST-1313422, AST-1413600, AST-1518308, and AST-1815034, and the NASA grant 16-ADAP16-0232. The work of DS was carried out at the Jet Propulsion Laboratory, California Institute of Technology, under a contract with NASA.

NPR acknowledges support from the STFC and the Ernest Rutherford Fellowship scheme.

This work made use of the Million Quasars Catalogue.

Funding for SDSS-III has been provided by the Alfred P. Sloan Foundation, the Participating Institutions, the National Science Foundation, and the U.S. Department of Energy Office of Science. The SDSS-III web site is http://www.sdss3.org/.

This publication makes use of data products from the Near-Earth Object Wide-field Infrared Survey Explorer (NEOWISE), which is a project of the Jet Propulsion Laboratory/California Institute of Technology. NEOWISE is funded by the National Aeronautics and Space Administration.

SDSS-III is managed by the Astrophysical Research Consortium for the Participating Institutions of the SDSS-III Collaboration including the University of Arizona, the Brazilian Participation Group, Brookhaven National Laboratory, Carnegie Mellon University, University of Florida, the French Participation Group, the German Participation Group, Harvard University, the Instituto de Astrofisica de Canarias, the Michigan State/Notre Dame/JINA Participation Group, Johns Hopkins University, Lawrence Berkeley National Laboratory, Max Planck Institute for Astrophysics, Max Planck Institute for Extraterrestrial Physics, New Mexico State University, New York University, Ohio State University, Pennsylvania State University, University of Portsmouth, Princeton University, the Spanish Participation Group, University of Tokyo, University of Utah, Vanderbilt University, University of Virginia, University of Washington, and Yale University.

REFERENCES

Abolfathi B. et al., 2018, ApJS, 235, 42
Aretxaga I., Joguet B., Kunth D., Melnick J., Terlevich R. J., 1999, ApJ, 519, L123
Assef R. J., Stern D., Noirot G., Jun H. D., Cutri R. M., Eisenhardt P. R. M., 2018, ApJS, 234, 23
Bellm E. C. et al., 2019, PASP, 131, 018002
Bischoff K., Kollatschny W., 1999, A&A, 345, 49
Charlton P. J. L., Ruan J. J., Haggard D., Anderson S. F., Eracleous M., MacLeod C. L., Runnoe J. C., 2019, ApJ, 876, 75
Cohen R. D., Rudy R. J., Puetter R. C., Ake T. B., Foltz C. B., 1986, ApJ, 311, 135
Davis S. W., Stone J. M., Pessah M. E., 2010, ApJ, 713, 52
Denney K. D. et al., 2014, ApJ, 796, 134
Drake A. J. et al., 2009, ApJ, 696, 870
Drake A. J. et al., 2013, ApJ, 763, 32
Drake A. J. et al., 2014, ApJS, 213, 9
Drake A. J., Djorgovski S. G., Graham M. J., Stern D., Mahabal A. A., Catelan M., Christensen E., Larson S., 2019, MNRAS, 482, 98
Eracleous M., Halpern J. P., 2001, ApJ, 554, 240

Gaskell C. M., Bartel K., Deffner J. N., Xia I., 2019, preprint (arXiv:1909.06275)
Gezari S. et al., 2017, ApJ, 835, 144
Graham M. J., Djorgovski S. G., Drake A. J., Mahabal A. A., Chang M., Stern D., Donalek C., Glikman E., 2014, MNRAS, 439, 703
Graham M. J. et al., 2015a, Nature, 518, 74
Graham M. J. et al., 2015b, MNRAS, 453, 1562
Graham M. J., Djorgovski S. G., Drake A. J., Stern D., Mahabal A. A., Glikman E., Larson S., Christensen E., 2017, MNRAS, 470, 4112
Graham M. J. et al., 2019, PASP, 131, 8001
Hirose S., Blaes O., Krolik J. H., 2009, ApJ, 704, 781
Ho L. C., Kim M., 2015, ApJ, 809, 123
Hook I. M., McMahon R. G., Boyle B. J., Irwin M. J., 1994, MNRAS, 268, 305
Hutsemékers D., Agís González B., Sluse D., Ramos Almeida C., Acosta Pulido J.-A., 2017, A&A, 604, L3
Hutsemékers D., Agís González B., Marin F., Sluse D., Ramos Almeida C., Acosta Pulido J.-A., 2019, A&A, 625, A54
Jarosik N. et al., 2011, ApJS, 192, 14
Jun H. et al., 2015, ApJ, 814, L12
Kasliwal V. P., Vogeley M. S., Richards G. T., 2015, MNRAS, 451, 4328
Kelly B. C., Bechtold J., Siemiginowska A., 2009, ApJ, 698, 895
Khachikian E.-Y., Weedman D. W., 1971, ApJ, 164, L109
Kim D.-C., Yoon I., Evans A. S., 2018, ApJ, 861, 51
King A. R., Pringle J. E., Livio M., 2007, MNRAS, 376, 1740
Kozłowski S., 2017, ApJS, 228, 9
Kynoch D., Ward M. J., Lawrence A., Bruce A. G., Landt H., MacLeod C. L., 2019, MNRAS, 485, 2573
LaMassa S. M. et al., 2015, ApJ, 800, 144
Lawrence A. et al., 2016, MNRAS, 463, 296
Li Y., Yuan W., Zhou H. Y., Komossa S., Ai Y. L., Liu W. J., Boisvert J. H., 2015, AJ, 149, 75
MacLeod C. L. et al., 2016, MNRAS, 457, 389
MacLeod C. L. et al., 2019, ApJ, 874, 8
Marin F., 2017, A&A, 607, 40
Massaro E., Maselli A., Leto C., Marchegiani P., Perri M., Giommi P., Piranomonte S., 2015, Ap&SS, 357, 75
Massey P., Gronwall C., 1990, ApJ, 358, 344
Matt G., Guainazzi M., Maiolino R., 2003, MNRAS, 342, 422
Moreno J., Vogeley M., Richards G., 2018, PASP, 131, 3001
Noda H., Done C., 2018, MNRAS, 480, 3898
Palaversa L. et al., 2013, AJ, 146, 101
Parker M. L. et al., 2016, MNRAS, 461, 1927
Parker M. L. et al., 2019, MNRAS, 483L, 88
Penston M. V., Perez E., 1984, MNRAS, 211, 33
Rivers E. et al., 2015a, ApJ, 804, 107
Rivers E. et al., 2015b, ApJ, 815, 55
Ross N. P. et al., 2018, MNRAS, 480, 4468
Ruan J. et al., 2016, ApJ, 826, 188
Rumbaugh N. et al., 2018, ApJ, 854, 160
Runco J. N. et al., 2016, ApJ, 821, 33
Runnoe J. et al., 2016, MNRAS, 455, 1691
Scargle J. D., Norris J. P., Jackson B., Chiang J., 2013, ApJ, 764, 167
Schlafly E. F., Finkbeiner D. P., 2011, ApJ, 737, 103
Schlegel D. J., Finkbeiner D. P., Davis M., 1998, ApJ, 500, 525
Selsing J., Fynbo J. P. U., Christensen L., Krogager J.-K., 2016, A&A, 585, A87
Shappee B. J. et al., 2014, ApJ, 788, 48
Shen Y. et al., 2011, ApJS, 194, 45
Sheng Z., Wang T., Jiang N., Yang C., Yan L., Dou L., Peng B., 2017, ApJ, 846, L7
Smith K. L., Mushotzky R. F., Boyd P. T., Malkan M., Howell S. B., Gelino D. M., 2018, ApJ, 857, 141
Sniegowska M., Czerny B., 2019, preprint (arXiv:1904.06767)
Stern D. et al., 2017, ApJ, 839, 106
Stern D. et al., 2018, ApJ, 864, 27
Stoehr F. et al., 2008, in Argyle R., Bunclark P., Lewis J., eds, ASP Conf. Ser. Vol. 394, Astronomical Data Analysis Software and Systems XVII. Astron. Soc. Pac., San Francisco, p. 505
Tohline J. E., Osterbrock D. E., 1976, ApJ, 210, L117
Wang J., Xu D. W., Wei J. Y., 2018, ApJ, 852, 26
Yang Q. et al., 2018, ApJ, 862, 109
Zu Y., Kochanek C. S., Kozłowski S., Udalski A., 2013, ApJ, 765, 106

SUPPORTING INFORMATION

Supplementary data are available at *MNRAS* online.

Figure B1. Light curves and spectra of CSQs identified in this paper.

Please note: Oxford University Press is not responsible for the content or functionality of any supporting materials supplied by the authors. Any queries (other than missing material) should be directed to the corresponding author for the article.

APPENDIX A: KNOWN CLQS

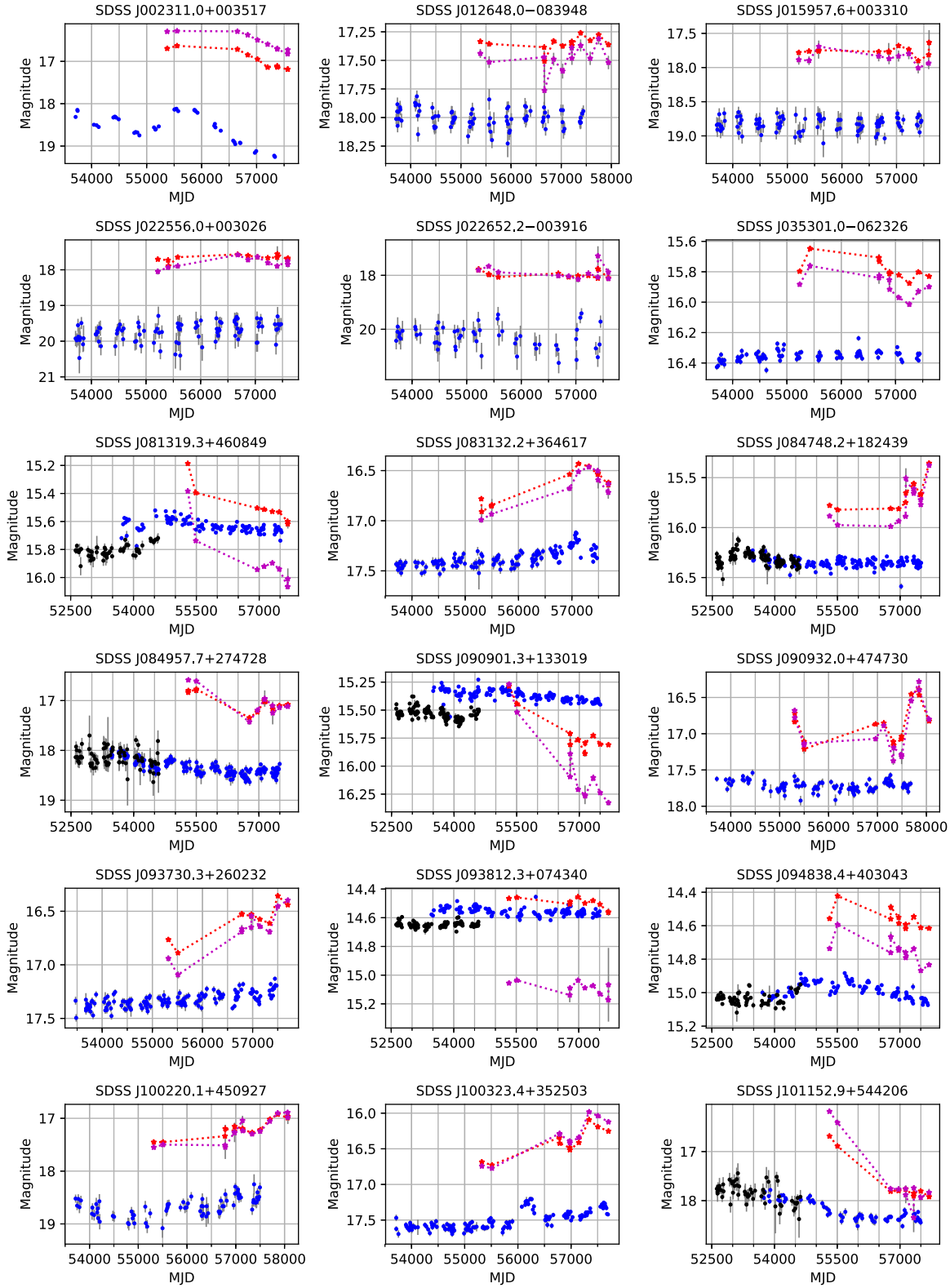

Figure A1. Light curves of CLQs identified in the literature showing the CRTS (blue) data and LINEAR (black) data where available. The *WISE* W1 (maroon) and W2 (red) light curves are also shown (binned on a daily basis) and offsets ($W1 = 2.70$, $W2 = 3.34$) have been applied to the *WISE* Vega magnitudes for display.

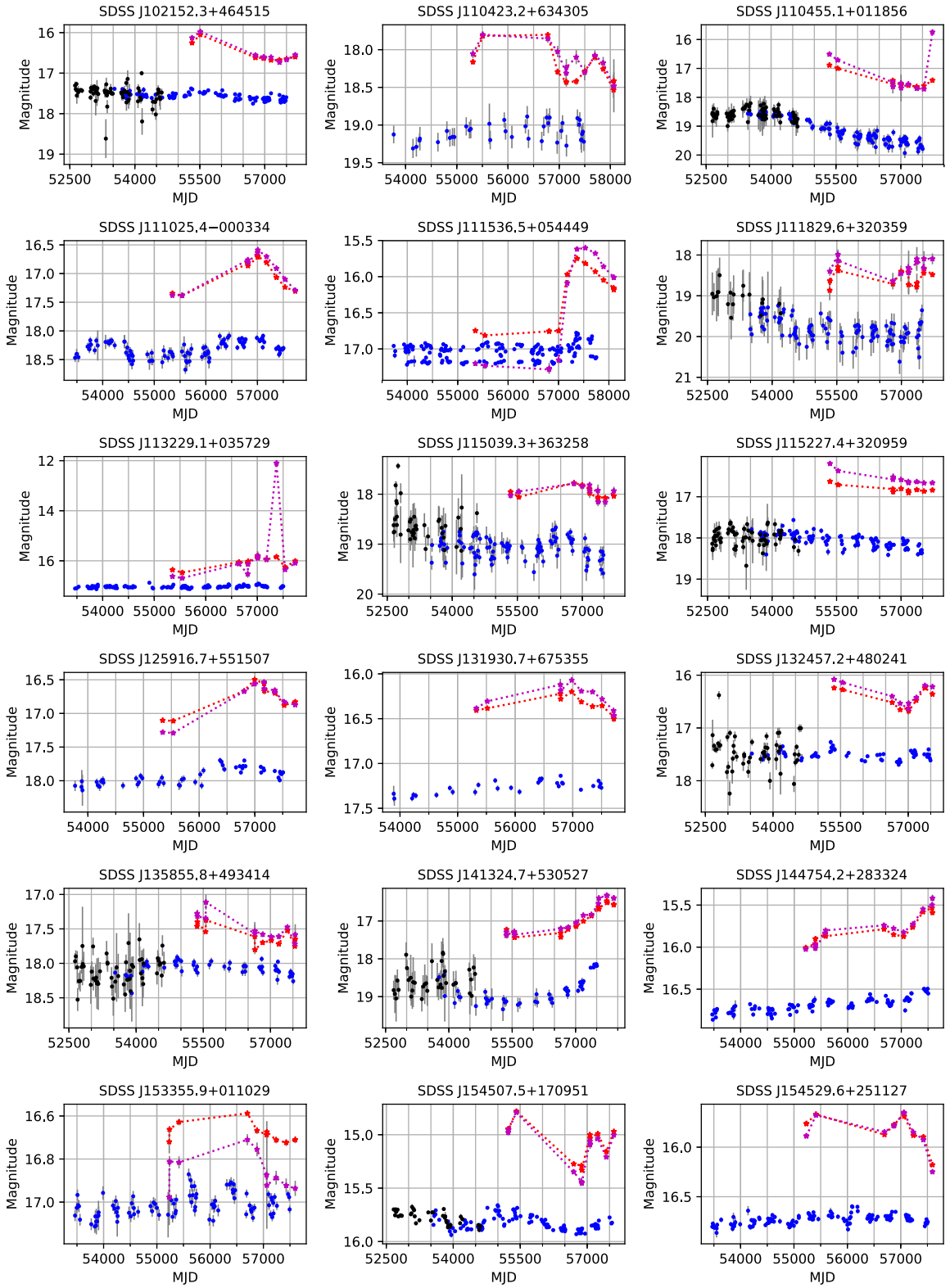

Figure A1 – *continued*

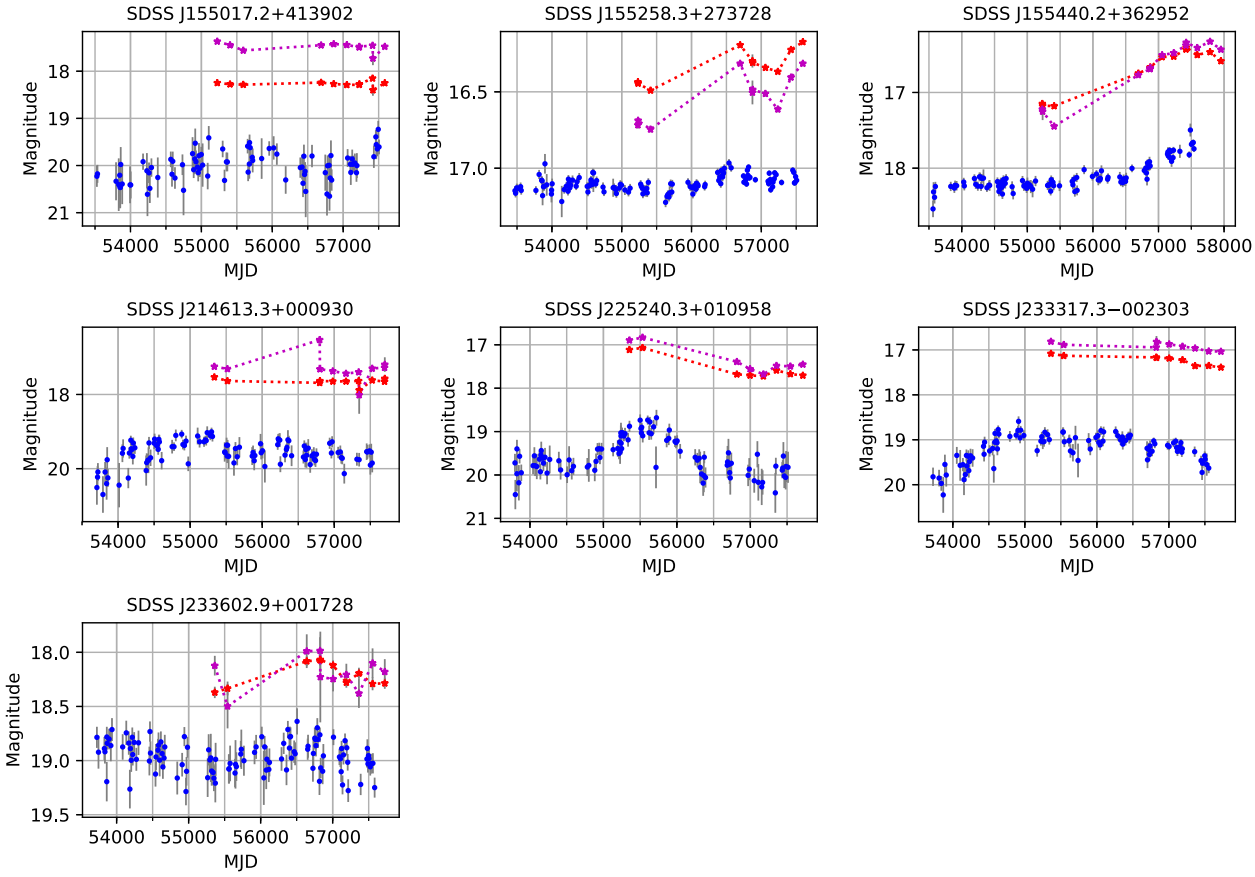

Figure A1 – *continued*.

Table A1. CLQs reported in the literature with CRTS coverage and associated features including the median CRTS magnitude (V_m), the optical amplitude (Amp), absolute change in $W1$, Bayesian block change (ΔBB), and Slepian wavelet variance measure (SWV_1). Sources marked with an asterisk have multi-epoch spectra in the public domain. SMBH virial mass estimates are calculated as described in Section 5.1 except for sources where no spectra are available.

Name	Transition	V_m (mag)	z	log (M_{BH}) ($M_\odot$)	Amp (mag)	$\lvert\Delta W1\rvert$ (mag)	ΔBB (mag)	SWV_1	Ref.
SDSS J000904.5−103428	Disappear	18.18	0.241	8.0	0.56	0.70	0.61	8.9	(12)
SDSS J002311.0+003517*	Appear	18.53	0.422	8.2	0.57	0.42	0.92	7.3	(1)
SDSS J004339.3+134437	Disappear	19.92	0.527	–	0.81	0.25	−0.18	2.3	(12)
SDSS J012648.0−083948	Disappear	18.00	0.198	7.8	0.21	0.10	0.03	1.3	(2)
SDSS J013458.3−091435*	Disappear	18.64	0.443	8.2	0.32	0.44	0.43	−4.0	(12)
SDSS J015957.6+003310*	Disappear	18.83	0.312	7.8	0.23	0.27	0	−15	(3)
SDSS J022556.0+003026*	Both	19.68	0.504	8.2	0.59	0.33	−0.19	3.9	(1)
SDSS J022652.2−003916*	Disappear	20.25	0.625	8.6	0.89	0.35	0.01	1.4	(1)
SDSS J035301.0−062326	Appear	16.35	0.076	7.6	0.10	0.23	−0.04	−13	(7)
SDSS J074511.9+380911	Disappear	17.84	0.237	9.1	0.19	0.20	0.13	−6.2	(12)
SDSS J081319.3+460849*	Appear	15.64	0.054	7.6	0.13	0.43	−0.05	−2.1	(7)
SDSS J083132.2+364617	Appear	17.40	0.195	–	0.21	0.48	−0.13	−5.1	(6)
SDSS J084748.2+182439	Disappear	16.35	0.085	7.7	0.18	0.47	0.18	−4.6	(7)
SDSS J084957.7+274728	Disappear	18.36	0.299	7.9	0.32	0.57	0.38	−0.1	(6)
SDSS J090902.3+133019	Appear	15.39	0.050	7.3	0.17	0.60	0.13	0.3	(7)
SDSS J090932.0+474730	Appear	19.14	0.117	–	0.19	0.82	0.08	9.9	(6)
SDSS J092702.3+043308	Disappear	17.93	0.322	–	0.29	0.49	0.18	7.7	(12)
SDSS J093730.3+260232*	Appear	17.33	0.162	7.6	0.18	0.53	−0.18	10	(6)
SDSS J093812.3+074340	Disappear	14.56	0.022	7.5	0.08	0.11	0.03	−2.8	(7)
SDSS J094838.4+403043	Disappear	14.99	0.047	7.5	0.10	0.20	0.06	0.1	(7)
SDSS J100220.1+450927*	Disappear	18.66	0.400	6.3	0.42	0.52	−0.06	8.3	(1)
SDSS J100323.4+352503	Appear	17.54	0.119	7.3	0.25	0.64	−0.06	3.8	(6)
SDSS J101152.9+544206*	Disappear	18.30	0.246	7.9	0.37	1.24	0.45	−5.8	(4)
SDSS J102152.3+464515*	Disappear	17.58	0.204	7.8	0.19	0.63	0.27	−5.1	(1)
WISE J105203.5+151929	Disappear	18.95	0.302	7.9	0.73	0.72	0.93	2.5	(9)
SDSS J110057.7−005304*	Dis/appear	18.09	0.378	8.2	0.51	0.40	−0.27	8.1	(11)
SDSS J110423.2+634305	Disappear	19.10	0.164	6.8	0.21	0.67	−0.14	12	(6)
SDSS J110455.1+011856	Disappear	19.29	0.575	8.2	0.70	0.74	0.94	1.1	(6)
SDSS J111025.4−000334*	Appear	18.31	0.219	7.6	0.31	0.69	−0.13	0.5	(6)
SDSS J111329.6+531338*	Disappear	18.44	0.239	7.8	0.29	0.42	0.11	6.1	(12)
SDSS J111536.5+054449*	Appear	17.01	0.090	7.7	0.22	1.06	0.17	4.2	(6)
SDSS J111829.6+320359*	Disappear	19.85	0.365	7.7	0.69	0.58	−0.14	−2.2	(6)
SDSS J113229.1+035729	Appear	17.04	0.091	8.3	0.13	0.68	−0.06	−10	(6)
SDSS J115039.3+363258*	Disappear	19.06	0.340	7.9	0.49	0.31	−0.1	−0.4	(6)
SDSS J115227.4+320959	Disappear	18.19	0.374	8.1	0.34	0.27	0.56	−0.9	(6)
SDSS J123359.1+084211	Disappear	17.92	0.255	8.7	0.25	0.85	0.30	−11	(12)
SDSS J125916.7+551507	Appear	17.96	0.198	7.9	0.22	0.61	−0.18	−5.3	(6)
SDSS J131930.7+675355*	Appear	17.26	0.166	7.7	0.13	0.30	−0.12	−9.7	(6)
SDSS J132457.2+480241*	Disappear	17.51	0.272	8.0	0.21	0.44	0.06	−4.3	(1)
SDSS J135855.8+493414*	Appear	18.06	0.116	6.9	0.26	0.43	−0.01	−6.5	(6)
SDSS J141324.7+530527*	Appear	18.91	0.456	8.2	0.60	0.96	−0.26	5.3	(10)
WISEA J142846.7+172353	Disappear	17.44	0.104	7.6	0.19	1.24	0.06	−5.2	(8)
SDSS J144754.2+283324	Appear	16.69	0.163	7.8	0.18	0.47	−0.31	−2.2	(6)
SDSS J153355.9+011029*	Appear	17.02	0.143	7.9	0.12	0.14	−0.03	−8.7	(6)
SDSS J153612.8+034245	Disappear	18.08	0.365	8.2	0.44	0.65	0.50	4.3	(12)
SDSS J153734.0+461358	Disappear	18.92	0.378	8.0	0.31	0.24	0.25	−11	(12)
SDSS J154507.5+170951	Appear	15.84	0.048	7.4	0.14	0.55	−0.02	5.5	(7)
SDSS J154529.6+251127	Appear	16.72	0.117	7.5	0.13	0.52	−0.04	−6.0	(6)
SDSS J155017.2+413902	Appear	19.98	0.220	–	0.70	0.25	−0.62	−2.5	(6)
SDSS J155258.3+273728	Appear	17.10	0.086	–	0.13	0.32	−0.07	8.1	(6)
SDSS J155440.2+362952	Appear	18.17	0.237	–	0.52	0.77	−0.76	15	(5)
SDSS J160111.2+474509	Disappear	18.29	0.297	7.9	0.19	0.15	0.03	−12	(12)
SDSS J161711.4+063833	Disappear	17.32	0.229	8.0	0.65	0.48	0.80	14	(12)
SDSS J162415.0+455130	Disappear	19.31	0.481	8.1	0.45	0.29	0.63	−6.8	(12)
SDSS J210200.4+000501	Disappear	18.41	0.329	8.0	0.26	0.47	0.26	−5.3	(12)
SDSS J214613.3+000930*	Appear	19.55	0.621	8.3	0.84	0.35	−0.48	2.6	(1)
SDSS J220537.7−071114	Disappear	18.18	0.295	8.0	0.21	0.23	0.15	−8.3	(12)
SDSS J225240.3+010958*	Appear	19.62	0.534	8.2	0.89	0.66	0.13	8.5	(1)
SDSS J233317.3−002303*	Appear	19.12	0.513	8.3	0.82	0.31	−0.44	4.4	(1)
SDSS J233602.9+001728*	Disappear	18.95	0.243	7.7	0.32	0.30	0.15	−4.2	(2)
SDSS J235107.4−091318	Disappear	17.95	0.355	7.9	0.20	0.20	0.16	−7.3	(12)

Note. References: (1) MacLeod et al. (2016); (2) Ruan et al. (2016); (3) LaMassa et al. (2015); (4) Runnoe et al. (2016); (5) Gezari et al. (2017); (6) Yang et al. (2018); (7) Runco et al. (2016); (8) Assef et al. (2018); (9) Stern et al. (2018); (10) Wang, Xu & Wei (2018); (11) Ross et al. (2018); (12) MacLeod et al. (2019).

APPENDIX B: CLQ CANDIDATES

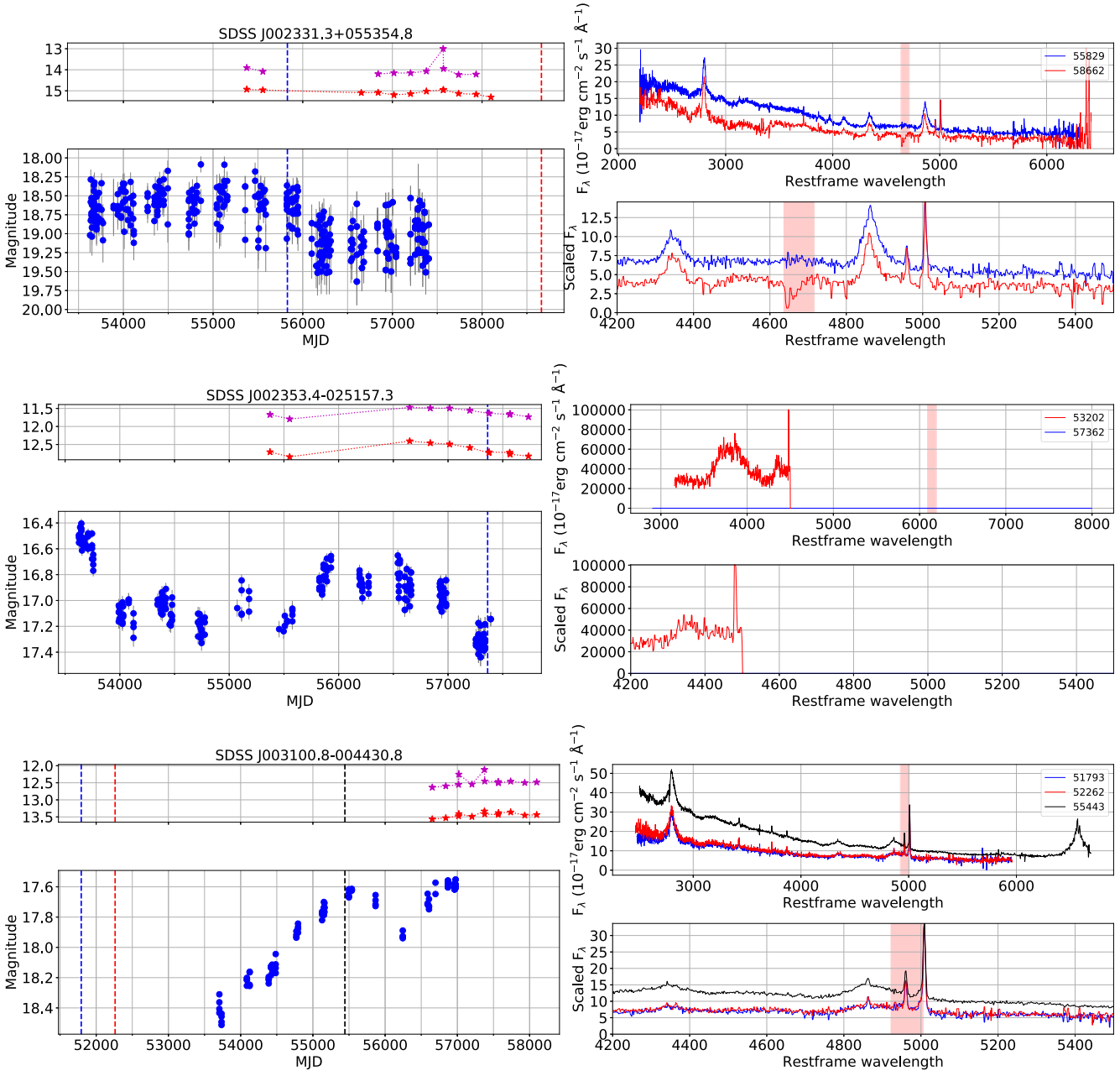

Figure B1. Light curves and spectra of CSQs identified in this paper. The lower left plot for each source shows the CRTS (blue) data and LINEAR (black) data where available. The *WISE* W1 (maroon) and W2 (red) light curves are also shown (binned on a daily basis) in the upper left plot. The right upper plot for each source shows the SDSS spectra and the spectra obtained in our follow-up. The lower right plot shows a comparison of the H β regions for the spectra scaled to the flux of [O III] λ 5007 in the earliest spectra. The spectra are smoothed with a 3 Å box filter in all cases. The red shaded area indicates the location of the atmospheric O_2 *A*-band absorption feature. The corresponding epochs of the spectra are shown in the left plot by dashed lines. The full set is available online.

Table B1. Spectroscopic observations of CSQ candidates. First epoch spectra are from SDSS; subsequent epoch spectra are from SDSS, Palomar (DBSP), and Keck (LRIS, ESI) as described in the text.

Name	First epoch (MJD)	Subsequent epochs (MJD)
SDSS J002331.3+055354.8	55829	58662 (DBSP)
SDSS J002353.5−025159.1	57362	58054 (DBSP)
SDSS J005346.1+223221.9	56904	58348 (DBSP)
SDSS J011919.3−093721.6	52163	58013 (DBSP)
SDSS J012326.8+241844.1	55885	58662 (DBSP)
SDSS J022014.6−072859.3	52162	57360 (DBSP)
SDSS J024533.6+000745.2	52177	52946 (SDSS), 56273 (SDSS), 56572/6 (SDSS), 56602 (SDSS), 58013 (DBSP)
SDSS J025003.0+010930.7	52177	52295 (SDSS), 57690/8 (DBSP), 57779 (DBSP)
SDSS J025410.1+034912.5	55477	57399 (SDSS)
SDSS J025505.7+002523.5	51816	51877 (SDSS), 52175 (SDSS), 58013 (DBSP)
SDSS J025619.0+004501.0	51816	51877 (SDSS), 52175 (SDSS), 56984 (SDSS), 58054 (DBSP), 58070 (DBSP)
SDSS J074542.3+421404.5	51885	58054 (DBSP)
SDSS J074819.0+335311.0	52237	52577 (SDSS), 58069 (DBSP)
SDSS J075440.3+324105.1	52583	57461 (ESI)
SDSS J075728.3+245510.1	52669	57698 (DBSP)
SDSS J080138.7+423355.2	55178	55245 (SDSS), 57073 (SDSS)
SDSS J080500.3+340225.6	52584	57698 (DBSP)
SDSS J081425.9+294116.3	52618	55542 (SDSS)
SDSS J081632.1+404804.6	52264	57361 (SDSS)
SDSS J082033.3+382420.4	52589	58212 (DBSP)
SDSS J082930.7+272821.9	52932	57698 (DBSP)
SDSS J083111.6+345928.1	52668	58212 (DBSP)
SDSS J083225.3+370736.6	52312	57050 (ESI)
SDSS J083236.3+044506.2	52646	57698 (DBSP)
SDSS J083533.2+494818.8	55290	58212 (DBSP)
SDSS J084716.1+373218.7	52323	57452 (SDSS)
SDSS J091357.3+052229.8	52652	57844 (DBSP), 58154 (DBSP)
SDSS J092441.1+284730.6	53389	57050 (ESI)
SDSS J092736.7+153824.3	54068	58131 (DBSP)
SDSS J092836.9+474245.8	52637	56740 (SDSS)
SDSS J093017.7+470721.7	52316	56685 (SDSS), 58131 (DBSP)
SDSS J093329.0+291734.1	53389	58131 (DBSP)
SDSS J094231.7+233613.6	53735	58069 (SDSS)
SDSS J094620.9+334746.5	53387	57461 (ESI), 57844 (DBSP)
SDSS J095427.6+485638.9	52703/8	58131 (DBSP), 58154 (DBSP)
SDSS J095536.8+103751.7	52996	57050 (ESI), 57844 (DBSP)
SDSS J095750.0+530106.0	52385	52400 (SDSS), 56993 (SDSS), 57844 (DBSP)
SDSS J100256.2+475027.9	52339	56338 (SDSS), 58154 (DBSP)
SDSS J100343.3+512611.2	52385	52400 (SDSS), 58246 (DBSP)
SDSS J102614.0+523752.0	52644	58212 (DBSP)
SDSS J102752.4+421012.5	55588	58154 (DBSP)
SDSS J102817.7+211508.1	53741	58154 (DBSP)
SDSS J103255.9+365451.0	55575	58246 (DBSP)
SDSS J104254.8+253714.2	53792	56358 (SDSS)
SDSS J105907.2+472331.5	52643	58201 (DBSP)
SDSS J110349.2+312416.7	53472	56367 (SDSS)
SDSS J110501.3+562723.8	52373	57374 (SDSS), 58212 (DBSP)
SDSS J111617.8+251035.0	54115	58246 (DBSP)
SDSS J111930.4+312416.7	50494	54178 (SDSS), 56304 (SDSS), 58154 (DBSP)
SDSS J111947.6+233539.9	54154	56304 (SDSS), 58212 (DBSP)
SDSS J112243.1+364141.6	53467	58212 (DBSP)
SDSS J113111.1+373709.4	53446	57426 (SDSS), 57844 (DBSP)
SDSS J113706.9+013948.2	51989	57461 (ESI)
SDSS J113757.7+365501.8	55673	57427 (SDSS)
SDSS J114408.9+424357.5	53062	57520 (SDSS)
SDSS J115349.3+112830.4	47939	53144 (SDSS), 57844 (DBSP)
SDSS J120130.9+494049.8	52442	54849 (SDSS), 58212 (DBSP)
SDSS J120442.2+275411.6	53819	56337 (SDSS), 58212 (DBSP)
SDSS J122136.8+343541.4	53503	58246 (DBSP)
SDSS J122503.4+293931.0	53287	57926 (DBSP)
SDSS J123001.0+335901.6	53819	57926 (LRIS)

Table B1 – *continued*

Name	First epoch (MJD)	Subsequent epochs (MJD)
SDSS J123203.6+200929.5	47527	54481 (SDSS), 58694 (DBSP)
SDSS J123215.2+132032.3	53166	58131 (DBSP), 58154 (DBSP)
SDSS J123819.6+412420.4	53090	57511 (SDSS)
SDSS J125327.7+145456.2	53498	58201 (DBSP)
SDSS J130749.6+350140.4	53799	57926 (LRIS)
SDSS J134133.7+090356.3	53886	58154 (DBSP)
SDSS J134628.4+192243.3	54507	58662 (DBSP)
SDSS J134822.3+245650.4	53535	58212 (DBSP)
SDSS J135636.6+255320.0	53792	58245 (DBSP), 58249 (DBSP)
SDSS J135820.4+134345.9	53883	57926 (DBSP)
SDSS J140506.2+171708.4	54509	57421 (DBSP), 57844 (DBSP)
SDSS J141403.2+352311.6	53143	58694 (DBPS)
SDSS J141758.6+091608.7	53794	58662 (DBSP)
SDSS J142725.0+194952.3	54534	58662 (DBSP)
SDSS J142852.8+271042.9	56067	57844 (DBSP), 58339 (DBSP)
SDSS J143919.4+551318.2	52668	54909 (SDSS), 58662 (DBSP)
SDSS J144118.9+485454.8	52733	56370 (SDSS), 58246 (DBSP)
SDSS J144202.8+433709.1	52734	57844 (DBSP)
SDSS J144702.8+273747.2	54208	57844 (DBSP), 57930 (DBSP)
SDSS J145022.7+102555.8	53827	57244 (DBSP), 57535 (DBSP)
SDSS J145440.4+552432.9	52343	58662 (DBSP)
SDSS J145450.0+111433.6	53521	57902 (DBSP)
SDSS J145755.4+435035.5	52734	58249 (LRIS)
SDSS J150332.1+295024.0	54138	58662 (DBSP)
SDSS J151604.3+355025.4	53083	57930 (DBSP)
SDSS J152641.9+163246.3	54266	58662 (DBSP)
SDSS J152749.9+084408.6	56002	57570 (DBSP)
SDSS J153354.6+345504.6	53144	57570 (DBSP)
SDSS J153415.4+303434.5	53119	57930 (DBSP)
SDSS J153926.8+200256.1	54232	58695 (DBSP)
SDSS J155651.4+321008.9	52825	58246 (DBSP)
SDSS J155829.4+271714.3	52817	57926 (LRIS)
SDSS J160007.4+111316.5	54572	58348 (DBSP)
SDSS J160030.3+264517.2	52822	58622 (DBPS)
SDSS J160743.0+432817.1	52756	57244 (DBSP), 57902 (DBSP), 57930 (DBSP)
SDSS J160848.2+004148.9	51690	58662 (DBSP)
SDSS J161400.3−011005.1	51693	57535 (DBSP)
SDSS J161413.2+260415.8	48004	52824 (SDSS), 57993 (DBSP)
SDSS J162552.8+125316.6	53881	58662 (DBSP)
SDSS J163523.4+263046.7	52824	58662 (DBSP)
SDSS J171602.0+311214.1	50551	52431 (SDSS), 58013 (DBSP)
SDSS J205032.3−070131.3	52145	52549 (SDSS), 58662 (DBSP)
SDSS J224829.4+144418.4	52263	57188 (DBSP), 57570 (DBSP), 58013 (DBSP), 57926 (LRIS), 58285 (LRIS)
SDSS J230443.6−084110.0	52258	58013 (DBSP)
SDSS J230702.9+043257.0	48152	58339 (DBSP)
SDSS J231207.6+140212.8	52251	57660 (DBSP)
SDSS J232256.7+185816.6	50359	56947 (SDSS), 58662 (DBSP)
SDSS J232446.7+140029.5	56209	58662 (DBSP)
SDSS J233136.8−105638.0	52523	57660 (DBSP)
SDSS J235439.1+005751.9	51788	52523 (SDSS), 56959 (SDSS), 58054 (DBSP)

This paper has been typeset from a TEX/LATEX file prepared by the author.